Laser powder bed fusion (LPBF) of NiTi alloy using elemental powders: the influence of remelting on printability and microstructure

Agnieszka Chmielewska
Faculty of Materials Science and Engineering, Warsaw University of Technology, Warsaw, Poland and
Department of Materials Science and Engineering, The Ohio State University, Columbus, Ohio, USA
Bartlomiej Adam Wysocki
Center of Digital Science and Technology, Cardinal Stefan Wyszyński University, Warsaw, Poland and
Additive Manufacturing Research Center, College of Engineering, Youngstown State University, Youngstown, Ohio, USA
Elżbieta Gadalińska
Materials and Structures Research Center, Łukasiewicz Research Network – Institute of Aviation, Warsaw, Poland
Eric MacDonald
W.M. Keck Center for 3D Innovation, University of Texas at El Paso, El Paso, Texas, USA
Bogusława Adamczyk-Cieślak
Faculty of Materials Science and Engineering, Warsaw University of Technology, Warsaw, Poland
David Dean
Department of Plastic and Reconstructive Surgery, The Ohio State University, Columbus, Ohio, USA and
Department of Materials Science and Engineering, The Ohio State University, Columbus, Ohio, USA, and
Wojciech Świeszkowski
Faculty of Materials Science and Engineering, Warsaw University of Technology, Warsaw, Poland

Abstract

Purpose – The purpose of this paper is to investigate the effect of remelting each layer on the homogeneity of nickel-titanium (NiTi) parts fabricated from elemental nickel and titanium powders using laser powder bed fusion (LPBF). In addition, the influence of manufacturing parameters and different melting strategies, including multiple cycles of remelting, on printability and macro defects, such as pore and crack formation, have been investigated.

Design/methodology/approach – An LPBF process was used to manufacture NiTi alloy from elementally blended powders and was evaluated with the use of a remelting scanning strategy to improve the homogeneity of fabricated specimens. Furthermore, both single melt and up to two remeltings were used.

Findings – The results indicate that remelting can be beneficial for density improvement as well as chemical and phase composition homogenization. Backscattered electron mode in scanning electron microscope showed a reduction in the presence of unmixed Ni and Ti elemental powders in response to increasing the number of remelts. The microhardness values of NiTi parts for the different numbers of melts studied were similar and ranged from 487 to 495 HV. Nevertheless, it was observed that measurement error decreases as the number of remelts increases, suggesting an increase in chemical and phase composition homogeneity. However, X-ray diffraction analysis revealed the presence of multiple phases regardless of the number of melt runs.

Originality/value – For the first time, to the best of the authors' knowledge, elementally blended NiTi powders were fabricated via LPBF using remelting scanning strategies.

Keywords Nickel-titanium (NiTi), Nitinol, Laser powder bed fusion (PBF), Selective laser melting (SLM), Remelting, Elemental powders, Premix powders, Laser powder bed fusion

Paper type Research paper

The authors are grateful to Dr M.J. Benzakein from The Ohio State University for linguistic proofreading.

(*continued on next page*)

Received 26 August 2021
Revised 28 December 2021
Accepted 14 February 2022

The current issue and full text archive of this journal is available on Emerald Insight at: **https://www.emerald.com/insight/1355-2546.htm**

Rapid Prototyping Journal
28/10 (2022) 1845–1868
Emerald Publishing Limited [ISSN 1355-2546]
[DOI 10.1108/RPJ-08-2021-0216]

1. Introduction

Additive manufacturing (AM) has now become a cost-effective, energy efficient and environmentally friendly fabrication process for low volume production. With the ongoing rapid reduction in three-dimensional (3D) printing costs, AM could soon become competitive with mainstream manufacturing forming strategies for mid-level runs as well. Due to geometric freedom, AM has been extensively developed during the past few years and has become the fastest growing manufacturing technique recently, particularly important with metallic materials (Bandyopadhyay and Bose, 2015; Gibson *et al.*, 2015; Weller *et al.*, 2015). The use of AM may significantly reduce or even eliminate the need for machining. Powder bed fusion (PBF) technology uses a laser or electron beam energy source to build parts by melting a metallic powder in a layer-wise manner. Compared to other nonpowder-bed metal AM systems, such as directed energy deposition or laser engineered net shaping, PBF has an advantage when used to fabricate parts with complex, including high porosity, geometries with both high resolution and high accuracy relative to the original computer-aided design (CAD) part's dimensions. However, one of the limitations of PBF is the low availability of suitable metallic powders from the small number of 3D printable alloys.

Shape memory alloys (SMA) show great potential in many aerospace and medical applications, and consequently are proving to be of great interest to AM (Dhanasekaran *et al.*, 2018; Farber *et al.*, 2019). Nickel-titanium (NiTi), also referred to as nitinol, is one of the well-known, and frequently used, SMA materials. Humbeeck (1999) and Sharma and Srinivas (2019) report that, in the aerospace industry, nitinol has been used to produce portions of aircraft wings. Furthermore, as reported by Duerig *et al.* (1999), Elahinia *et al.* (2012) and Chen *et al.* (2019), nitinol is an essential material in the medical device engineer's toolbox and, is widely used in various biomedical engineering applications, such as orthodontic arch wires, surgical stents, active catheters, spine-fracture fixations, oral and maxillofacial implants, bone plates and lumbar vertebral replacements.

NiTi's unique mechanical properties result from reversible, solid-state, phase transformations that occur when the material is subject to external stimuli such as a change in temperature or an applied stress. A phase transformation induced by a change in temperature is the mechanism responsible for the shape memory property, while transformation-induced by stress are the mechanisms that initiate a part's superelastic property. This diffusionless martensitic transformation occurs between the parent B2 austenite phase and the B19' martensitic phase. The superelastic and shape memory responses simply depend on the transformation temperature of the NiTi component coupled with the ambient temperature. Dadbakhsh *et al.* (2014) and Frenzel *et al.* (2010) demonstrated that below the martensite finish (M_f) temperature, the NiTi alloys will exhibit shape memory, while above the austenite finish (A_f) temperature, the NiTi material will exhibit superelasticity. The martensitic transformation temperature is sensitive to the alloying ratio. Khalil-Allafi and Amin-Ahmadi (2009) described that the martensite start (M_s) temperature varies significantly with atomic percent change in Ni content. For this reason, it is possible to precisely control the transformation temperature by selecting the appropriate chemical composition of the material, as reported by Dadbakhsh *et al.* (2014) and Frenzel *et al.* (2010). There are a limited number of NiTi powders with different chemical compositions on the market. Therefore, if there is a need to obtain a material with a specific chemical composition, the powder must be produced, which is a time-consuming and expensive process. Hence, *in situ* alloying via AM from elemental powders is a promising, cost-effective alternative, which offers the flexibility to tailor the powder composition. The enhanced ability to vary and control laser powder bed fusion (LPBF) nitinol part material properties may lead to the creation of novel alloys.

To overcome the problems related to preparation of the powders with different relative Wt. % compositions of either Ni or Ti, AM manufacturing from elementally blended powders has been implemented. Thus far, studies presented by Stoll *et al.* (2020), Wang *et al.* (2019), Zhao *et al.* (2020) and Zhang *et al.* (2013) have previously shown the potential of using LPBF to synthesize NiTi alloys directly from elementally blended pure nickel and titanium powders. Those studies demonstrated that fabrication parameters influence microstructure and mechanical properties as well as phase formation. Moreover, it was reported by Zhang *et al.* (2013) and Zhao *et al.* (2020) that energy input influences phase transition in as-built LPBF-fabricated NiTi parts. Wang *et al.* (2020) subjected fabricated materials to postprocessing heat treatment to increase material homogeneity. This indeed reduced presence of unwanted phases and promoted formation of the NiTi phase.

In all of the previously mentioned studies on LPBF of NiTi parts from Ni and Ti elemental powders, different process parameters have been optimized, such as energy density, scan velocity and scanning vector rotation. Nevertheless, a remelting process, which is an additional melting process for a consolidated layer, without covering it with new metal powder, has not been yet examined for the LPBF of elemental Ni and Ti powders. Zhang *et al.* (2019) show that during the fabrication of NbMoTaW alloy parts from mixed multielement powders, use of a remelting strategy has a positive impact on the homogeneity of the material, and that homogeneity may be further improved via an "*in situ* heat treatment" which occurs during remelting of already solidified layers before the next layer is printed. Moreover, Wei *et al.* (2019) report that this phenomenon can eliminate thermal stress and inhibit crack initiation and propagation.

Fischer *et al.* (2016), Simonelli *et al.* (2018) and Vrancken *et al.* (2014) explored LPBF powder mix fabrication of different alloys where only basic LPBF parameters were adjusted during the manufacturing process. This resulted in the high inhomogeneity of fabricated materials when no remelting or laser focus variation was used. Therefore, given what has previously been studied in regard to LPBF of Ni and Ti elemental powders, the objective of the current study is to investigate the effect of remelting of each layer on the homogeneity of NiTi parts fabricated from elemental nickel and titanium powders via LPBF. In addition, the influence of manufacturing parameters (i.e. laser

Funding: The authors would like to thank the NCN (National Science Center) for providing financial support to project Synthesis and characterization of novel biomaterials based on 3D multifunctional titanium substrates (Grant No. 2017/25/B/ST8/01599). Dr Bartłomiej Wysocki would like to acknowledge grant provided by The Kosciuszko Foundation (www.thekf.org) – The American Centre of Polish Culture.

parameters and scanning strategy) and different melting strategies, including multiple remelting, on printability and the occurrence of macroscopic defects, such as pores and cracks, were investigated. Currently, there are two major limitations to using as-cast NiTi, machining difficulties and its high price. One major benefit of AM technologies is the reduction or elimination of the need for machining. Prealloyed NiTi powder used for AM is also expensive. Production Ni-Ti components using premixed Ni and Ti elemental powders, instead of prealloyed powders, would reduce the material costs of fabrication by nearly three times. Consequently, the price of the final part would be significantly reduced, thereby providing the possibility of wider application of this material in many industrial fields.

2. Materials and methods

2.1 Powder preparation

Spherical elemental powders of Ni (TLS Technik, Germany; size range <45 μm; D10 = 6.57 μm; D50 = 19.95 μm; D90 = 39.67 μm) and Ti (grade 1 TLS Technik; size range 15–45 μm; D10 = 14.68 μm; D50 = 30.58 μm; D90 = 44.24 μm) were used in this study. The Ni:Ti powder blend ratio was Ni 55.7 Wt.%: Ti 44.3 Wt.%. The chemical compositions, including impurities, of Ni and Ti are listed in Tables 1 and 2, respectively. The two powders were dry blended, without any additives or lubricants, in a tumbling mixer for 2 h to achieve uniform particle distribution. The morphology of the powders, as well as their distribution after blending, was observed in a Hitachi SU-8000 (Hitachi, Japan, Tokyo) scanning electron microscope (SEM).

2.2 Manufacturing

Cylindrical parts of dimensions $\phi 6 \times 4$ mm were fabricated in the LPBF process using a Realizer SLM50 machine (Realizer GmbH, Borchen, Germany) equipped with a ytterbium fiber laser source with a maximum power output of 120 W. The fabrication process was performed under an argon atmosphere while the oxygen content was kept below 0.3 Vol.%. The build parts were deposited on a substrate made from bulk NiTi to provide compatibility and wettability with the processed materials. The substrate was preheated and kept at 200°C to ensure building parts remained bonded to the substrate during the process. The process parameters were as follows: laser power (P) of 25–30 W, scanning speed (v) of 500–100 mm/s, hatch spacing (h) of 0.03–0.07 mm and hatch angle of 45° (no contours were applied). The powder layer thickness (t) was set to 25 μm. Based on the equation E = P/(vht), the energy density was calculated and varied in the range of 14–80 J/mm^3. The LPBF parameters optimization procedure (laser parameters and scanning strategies) for the parts fabrication are shown in Appendix 1.

After the first scan, here referred to as a single melting (SM), some sets of parts were subjected to one or two additional remeltings. This means that on each platform, every layer of the part was scanned one, two or three times, as shown in Figure 1. Each first and second remelting was performed in the same laser scanning direction as was used in the first melt. The remelting was processed with different parameters than the first melt. Two remelting parameters R1 and R2 were used, with scanning speeds of 1,000 and 3,000 mm/s and a laser power of 25 W and 75 W, respectively. Both parameters for remelting resulted in the same energy density of 33 J/mm^3. The use of those three melting strategies allowed to obtain five platforms of parts with the scanning parameters as described in Table 3.

Table 1 Chemical composition of nickel powder

Element	Ni	C	Fe
Wt. [%]	99.9	0.017	<0.1

Table 2 Chemical composition of titanium powder

Element	Ti	C	Fe	N	H	O
Wt. [%]	Bal.	<0.08	<0.20	<0.03	<0.015	<0.18

2.3 Microstructure characterization and phase identification

After fabrication, parts were removed from the substrate and hot mounted in resin. All parts were mechanically ground and polished for further tests. Pore and crack density were studied on metallographically prepared specimens using light microscopy (Zeiss AxioScope Light Microscope). The relative density of the parts was calculated on the basis of microscopic images using MicroMeter software (Wejrzanowski *et al.*, 2008, 2010).

To reveal Ni and Ti elemental distribution in the 3D printed parts, parts were analyzed using a Hitachi SU-8000 SEM in the backscattered electron (BSE) mode. SEM BSE observations were performed to provide information about the distribution of different elements in the part according to their atomic number. The parts were subjected to scanning electron microscopy with energy dispersive spectroscopy (SEM-EDS) analysis to obtain elements maps for the evaluation of the homogenization ratio.

A qualitative phase analysis was performed by X-ray diffraction (XRD) at room temperature using a Bruker D8 Advance (Bruker, Germany) diffractometer with filtered Cu Kα (λ = 0.154056 nm) radiation. The recording conditions of the XRD patterns were as follows: voltage 40 kV, current 40 mA, angular range 2Θ from 30° to 110°, step $\Delta 2\Theta$ – 0.05°, counting time –3 s. The XRD patterns were analyzed using Bruker EVA software and the PDF-2 database (from the International Centre for Diffraction Data). The diffraction measurements of stress values were performed with a PANalytical Empyrean diffractometer with Cr Kα (λ = 0.228976 nm) radiation. The Kβ component of the radiation was cutoff by applying a V filter. The first attempts to obtain diffraction stress measurements were made using Cu Kα radiation for a NiTi (B2) phase reflection with *hkl* Miller coefficients (321), which nominally, according to the 04–017-0804 card of the ICDD PDF4+ libraries, should be at approximate position 2θ = 147.127°. Unfortunately, the multiplicity of planes with these coefficients turned out to be unsatisfactory to collect reliable stress measurements. When Cr radiation was used, it was possible to obtain higher peak intensities for reflections with *hkl* coefficients (211). The position of the reflex according to the referenced ICDD4+ card was 2θ = 137.881°. A disadvantage of the measurement for the material under investigation using Cr radiation was the appearance of a high amount of fluorescence. This phenomenon was compensated by using appropriate detector

Figure 1 Scheme of melting strategies used, including in some cases up to two remelts

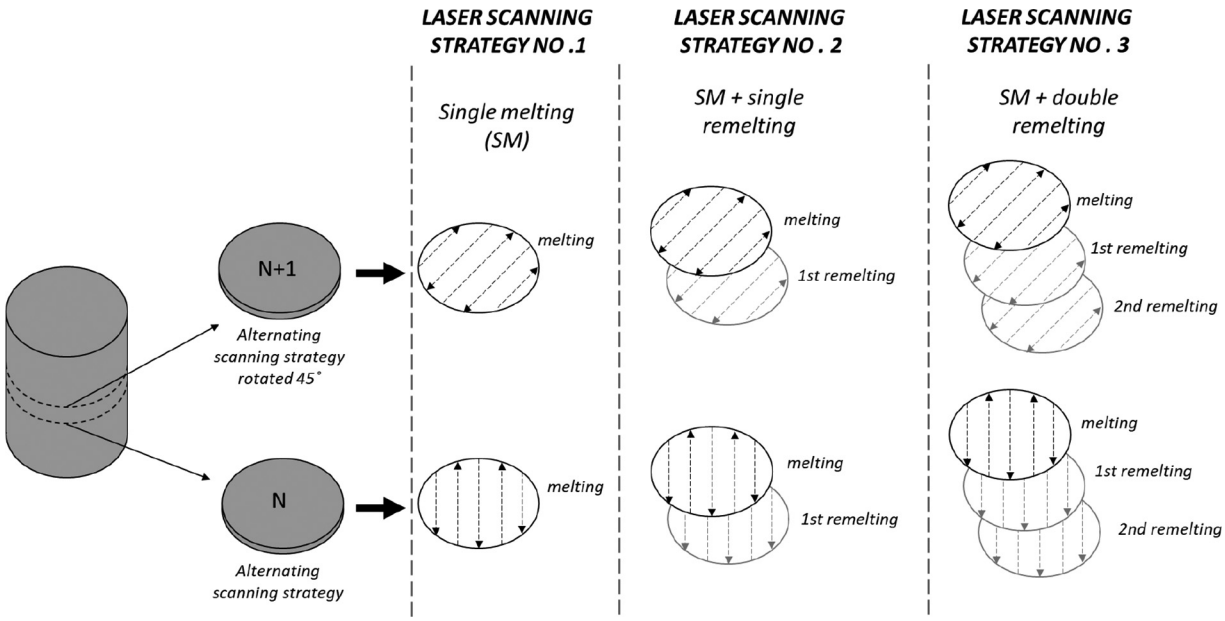

Table 3 LPBF process parameters and number of remelts used for processing of blended elemental Ni and Ti powders

Platform no.	Remelting no.	Melting	1st remelting	2nd remelting
1	Single melting (SM)	14–80 J/mm^3 (P = 25–30W, v = 500–1,000 mm/s)		
2	Single melting (SM) + one remelting	14–80 J/mm^3 (P = 25–30 W, v = 500–1,000mm/s)	33 J/mm^3 (R1) (P = 25 W, v = 1,000mm/s)	
3	Single melting (SM) + two remeltings	14–80 J/mm^3 (P = 25–30 W, v = 500–1,000mm/s)	33 J/mm^3 (R1) (P = 25 W, v = 1,000mm/s)	33 J/mm^3 (R1) (P = 25 W, v = 1,000mm/s)
4	Single melting (SM) + one remelting	14–80 J/mm^3 (P = 25–30 W, v = 500–1,000mm/s)	33 J/mm^3 (R2) (P = 75 W, v = 3,000mm/s)	
5	Single melting (SM) + two remeltings	14–80 J/mm^3 (P = 25–30 W, v = 500–1,000mm/s)	33 J/mm^3 (R2) (P = 75 W, v = 3,000mm/s)	33 J/mm^3 (R2) (P = 75 W, v = 3,000mm/s)

energy thresholds. The incident X-ray beam was collimated and made quasi-parallel using a polycapillary. The incident beam was limited to a size of 1 × 2 mm^2. Stress measurements were carried out in side-inclination geometry. The step for $\sin^2\psi$ was 0.15°, stress measurements were carried out for three directions relative to the specimen to obtain the information about the full stress tensor. Each measurement was made by collecting the shape and position of nine diffraction peaks. Each diffraction peak was observed in the angular range of 9.56°, the measurement step was 0.105° and the measurement for each peak lasted about 2 h.

The microhardness measurements on all parts were implemented on a polished XY plane using a microhardness tester (Falcon 500, Innovatest, The Netherlands). A load of 200 g and indentation time of 15 s was selected. For each part, six load test readings were taken at different locations and the average value was considered as a microhardness value.

A TCHEN 600 Nitrogen/Oxygen/Hydrogen determinator (LECO, St. Joseph, MI, USA) was used to determine the content of oxygen in all fabricated parts. The elements are converted to their oxidized form by using the gas fusion method, and the infrared absorption is used to measure combustion gases within a metallic part.

The chemical composition of the fabricated parts was analyzed using a ZSX Primus II (Rigaku, Japan) Wavelength Dispersive X-ray Fluorescence (WD-XRF) device.

The density of the selected parts was evaluated by the Archimedes method and μCT analysis. The μCT images were collected on a HeliScan (Thermo Fisher Scientific, Waltham, MA). The voxel size was set to 5.3 μm. A source voltage of 100 kV and a source current of 100 μA were used. A 3-mm aluminium filter material was chosen. The scanning procedure was carried out by rotating an emitted X-ray by 180°, 1,800 projections per resolution and an exposure time of 0.45 s per projection.

3. Results and discussion

3.1 Powder characterization

The powder mixture of elementally blended pure Ni and Ti is shown in Figure 2. SEM observation using a BSE signal shows

Figure 2 Powder mixture of elementally blended pure Ni and Ti powders

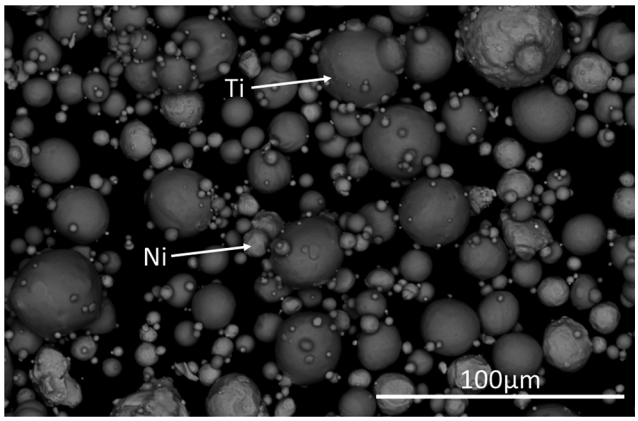

Ti particles that are darker with a smooth surface, while Ni particles are brighter and their surface is more irregular. The particles were uniformly distributed, and no agglomerates were observed.

3.2 Effects of processing parameters on printability

In this study, printability refers to successfully building apart, and concurrently avoiding or minimizing macrocracking defects and delamination. Lu *et al.* (2020) and Zhang *et al.* (2019) have reported that in their studies, when remelting was done at a different angle than the first scanning, with NiTi elementally blended powders, when changing the direction of remelting, the laser collects welding contaminations on the part surface. That collection of contaminations causes surface roughness and porosity. Liu and Guo (2020) and Sato *et al.* (2017) studied the occurrence of welding contamination. They found that welding contamination depends on manufacturing conditions, as well as used material and its morphology. In this study, during the first scanning of each layer (SM), the laser moved aside causing welding contamination, such as spatter particles and balling, and isolated the contaminants at the edge of fabricated layer [Figure 3(a)]. It was observed that after the direction of the remelting was changed (rotated in relation to the SM), and the laser approached the edge, where the welding contamination had accumulated, some of the contaminated agglomerations were observed to be collected by the laser and spread over the part's surface [Figure 3(b)]. Additionally, in the agglomerations caused high surface roughness and porosity in these parts (Appendix 1). However, when the direction of remelting was the same as in a SM fabricated part, the welding contaminations were limited to the edge of the fabricated layer, and its surface was smooth [Figure 3(c)]. Therefore, each first and second remelting was performed in the same direction as the first scan. Moreover, Li *et al.* (2012) observed that a remelting procedure can also alleviate the balling effect to a certain extent due to the melting and wetting of metal balls. Thus, remelting can improve surface quality.

Figure 3 Schematic illustration of a) the formation of contamination during the scanning and the influence of melting strategy on welding contamination, b) welding contamination collects at the edge of the printed part in each layer and c) the size of welding contamination expands as the part is built

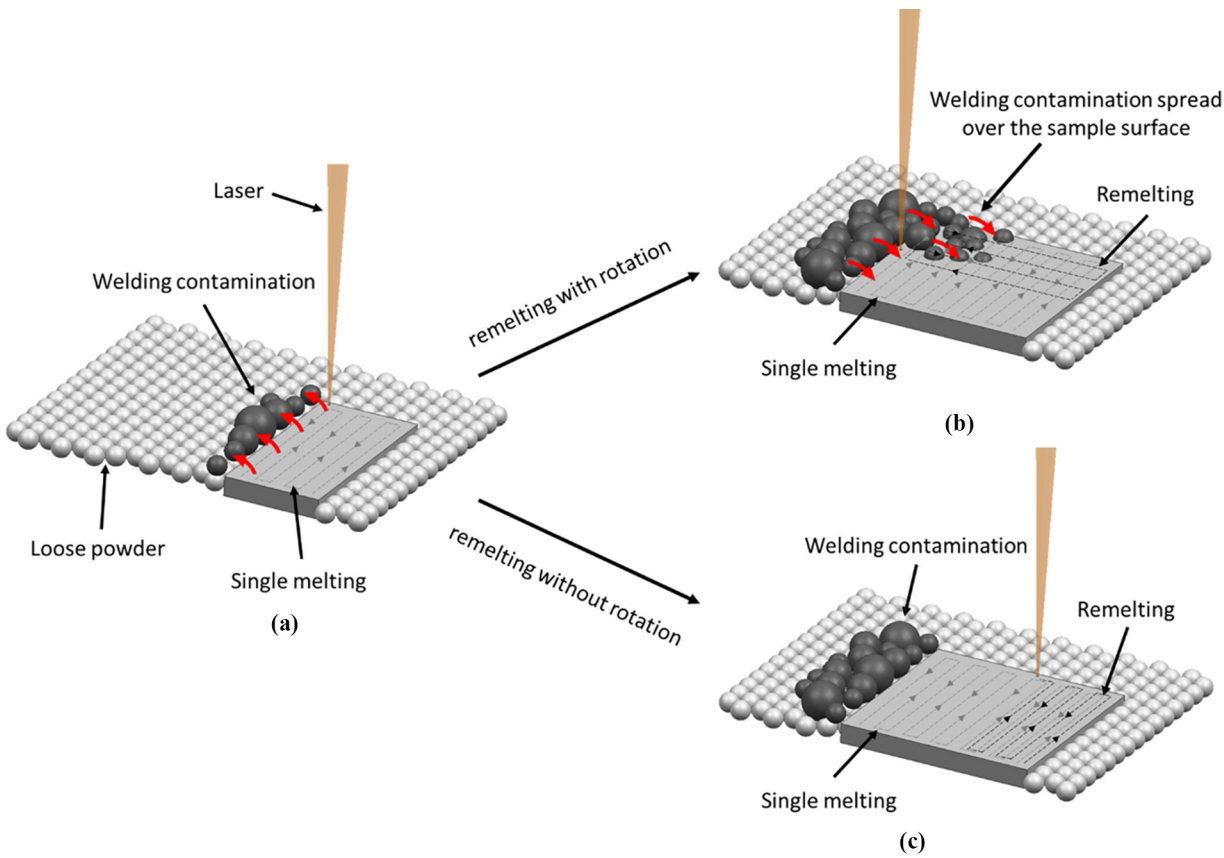

All of the samples manufactured in the separate substrates are shown in Figure 4. The manufacturing parameters used for SM, located on platform 1, enable the fabrication of parts free of macroscopic defects, as well as avoiding delamination and macrocracks. No significant dimensional inaccuracy (in macroscale) due to the powder adhesion was observed. The SM parts also showed no deformation due to high energy input. Therefore, all of the samples from platforms 2–5 were subjected to further remelting. Samples remelted with R1 parameters once and twice, shown on platforms 2 and 3, respectively, were free of macroscopic-defects, cracks or delamination. Instead, R2 remelting parameters induced minor cracks along the build direction. First and second R2 remelting are shown on platforms 4 and 5, respectively. Visible cracks could be the result of high temperature differences, stresses due to phase transitions or the formation of brittle phases, i.e. $NiTi_2$, Ni_3Ti and Ni_4Ti_3 (Chen, 2003; Motemani *et al.*, 2009; Thomas, 2015). SM parts as well as remelted parts with R1 parameters have smoother top surface, while those remelted with R2 parameters have a more irregular top surface. Moreover, some of the R2 remelted parts failed during the fabrication. The failure of the parts may be caused by the large thermal gradient that generates high thermal stresses as discussed in Section 3.3.

3.3 Microstructure

Figure 5 shows optical micrographs of a polished surface of parts fabricated with different energy densities and melting strategies. The presence of pores and cracks in the microstructure of the fabricated parts was observed. The size and distribution of pores, as well as cracks, depend on the manufacturing parameters. The porosity decreases with increasing energy density and with the remelting applied for most parts. Li *et al.* (2019) and Griffiths *et al.* (2018) reported that remelting provided good metallurgical bonding between adjacent melt pools and the formation of shallower melt pools. As a result, the density and surface quality was improved. Chen *et al.* (2018), Griffiths *et al.* (2018) and Xiong *et al.* (2020) discovered similar results in their works, where remelting was applied. It was reported that due to good metallurgical fusion provided by remelting, the pores were successfully reduced. Moreover, the number of pores and their average size were minimized.

For the majority of the parts rendered, the size of the pores decreases with applied remelting strategy. However, some combinations of first melting parameters and additional remelting resulted in a reduction in the number of pores while increasing their size. This phenomenon was mainly observed for parts fabricated at lower energy densities used for SM. It can be explained by the presence of lack-of-fusion zones which are observed for the parts produced with lower energy densities, which is likely due to narrower and shallower melt pools. It was reported by Dong *et al.* (2021) and Liu *et al.* (2021) that relatively low energy densities lead to poor fusion quality of laser tracks and massive lack-of-fusion zones were observed. As a result, the porosity seen in the parts manufactured with low energy densities is generated due to the incomplete fusion of the metal powder during laser scanning and the creation of lack of fusion. Thus, it can be concluded that the observed porosity results from the lack of fusion is correlated with decreasing energy density. This effect is even more obvious for AM systems where the laser exposure scanning track in the point distance mode in contrast to systems where the laser is working in a constant mode.

Wang *et al.* (2019) found that the increase of the energy density enhances microstructural homogeneity of the material and the disappearance of lack-of-fusion effects; however, spherical pores arise. High energy densities generate excess heat input that induces material evaporation. When the material evaporates the melt pool collapses, and spherical pores are formed. The process is called key-hole type melting and was previously reported by Ali *et al.* (2017), Liu *et al.* (2021) and Trapp *et al.* (2017). However, high energy input affects dimensional inaccuracy due to the phenomenon of surface adhesion of partially melted powder. Moreover, as described in previous studies by Chmielewska *et al.* (2019) and Tang *et al.* (2020), significant deformation of the fabricated parts has been observed under a high energy deposition fabrication process. Therefore, in this study, high energy densities have been replaced by remelting scanning strategies to eliminate the

Figure 4 Results of LPBF parts manufactured with different numbers of remelts

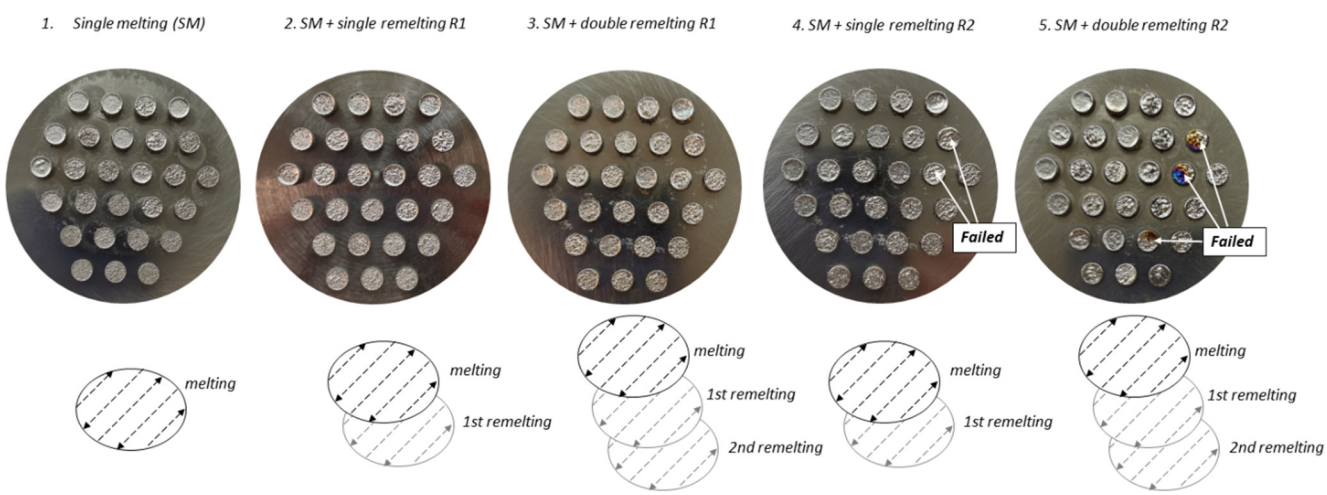

Figure 5 Light microscopy micrographs of parts manufactured with different process parameters and number of remelts

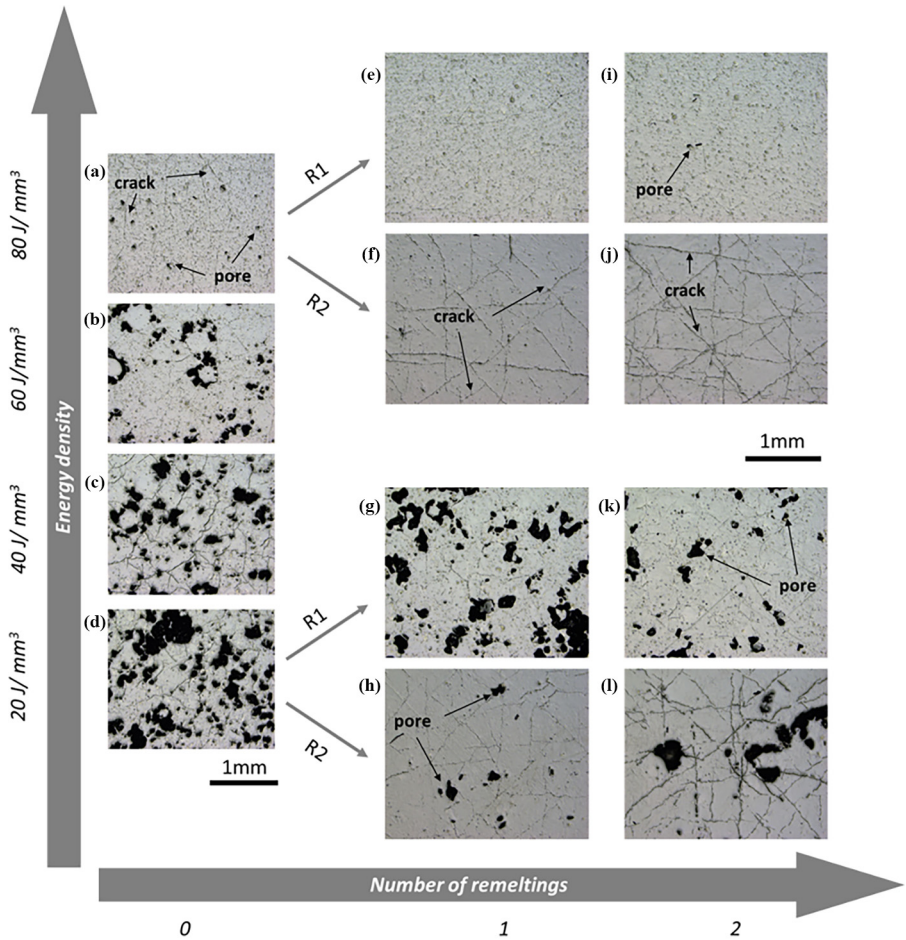

Notes: (a–d) As-built parts; (e) 80 J/mm³ + R1; (f) 80 J/mm³ + R2; (g) 20 J/mm³ + R1; (h) 20 J/mm³ + R2; (i) 80 J/mm³ + 2x R1; (j) 80 J/mm³ + 2x R2; (k) 20 J/mm³ + 2x R1; (l) 20 J/mm³ + 2x R2

formation of high-temperature defects and prevent dimensional inaccuracy.

Furthermore, cracks are visible for both SM and remelted parts. For R1 parameters, both the first and second remelting cause a significant reduction in the number of cracks or their complete elimination. For R2 parameters, the number of cracks visible in the material increases with an increasing number of remelts. Moreover, the cracks became distinct with large widths and lengths as a result of increasing the number of remelts. The emergence of the cracks may be related to the phenomenon of thermal stress during LPBF fabrication. Ali *et al.* (2017), Guo *et al.* (2019), Leuders *et al.* (2013) and Shi *et al.* (2020) have observed that when laser power and scanning velocity are high, rapid solidification and a large thermal gradient occur, resulting in high thermal stresses and thus the creation of cracks. With the lower laser power and scanning speed, the solidification rate and thermal gradient are lower; thus, lower thermal stresses occur or can be completely eliminated. This phenomenon is noticeable in the applied R1 and R2 remelting with the same energy densities generated by different values of the scanning speed and laser power. The scanning velocity and laser power for R2 was three times higher than in R1. Consequently, in the case of R2 remelting, more cracks were generated, while R1 remelting eliminated cracks. It can be concluded that laser power, as well as the scanning speed, should be well balanced to obtain low porosity and crack-free microstructure.

The densities calculated on the basis of microscopic observations correlate with different energy densities for all melting strategies are presented in Figure 6. The application of the remelting process improves material density and allows for fabrication of the parts with the density of up to 98.35%. Material density improves with higher energy densities of the first melting.

Remelting R1 resulted in higher densities of parts LPBF fabricated from Ni and Ti elemental powders than R2. This phenomenon may be related to the aforementioned higher temperature gradient in R2 remelting compared with R1. An inverse relationship is observed between the value of energy density and porosity. For the parts fabricated by SM with energy density below 20 J/mm³ high porosity and low material density, below 75%, was observed. Moreover, the use of R2 remelting resulted in significant cracks expansion, and an increase in cracks with the increasing number of remelts, as depicted in Figure 5. Ali *et al.* (2017), Guo *et al.* (2019),

Figure 6 Relationship between relative density and energy density for NiTi manufactured with elementally blended powders (raw data presented in Appendix 2)

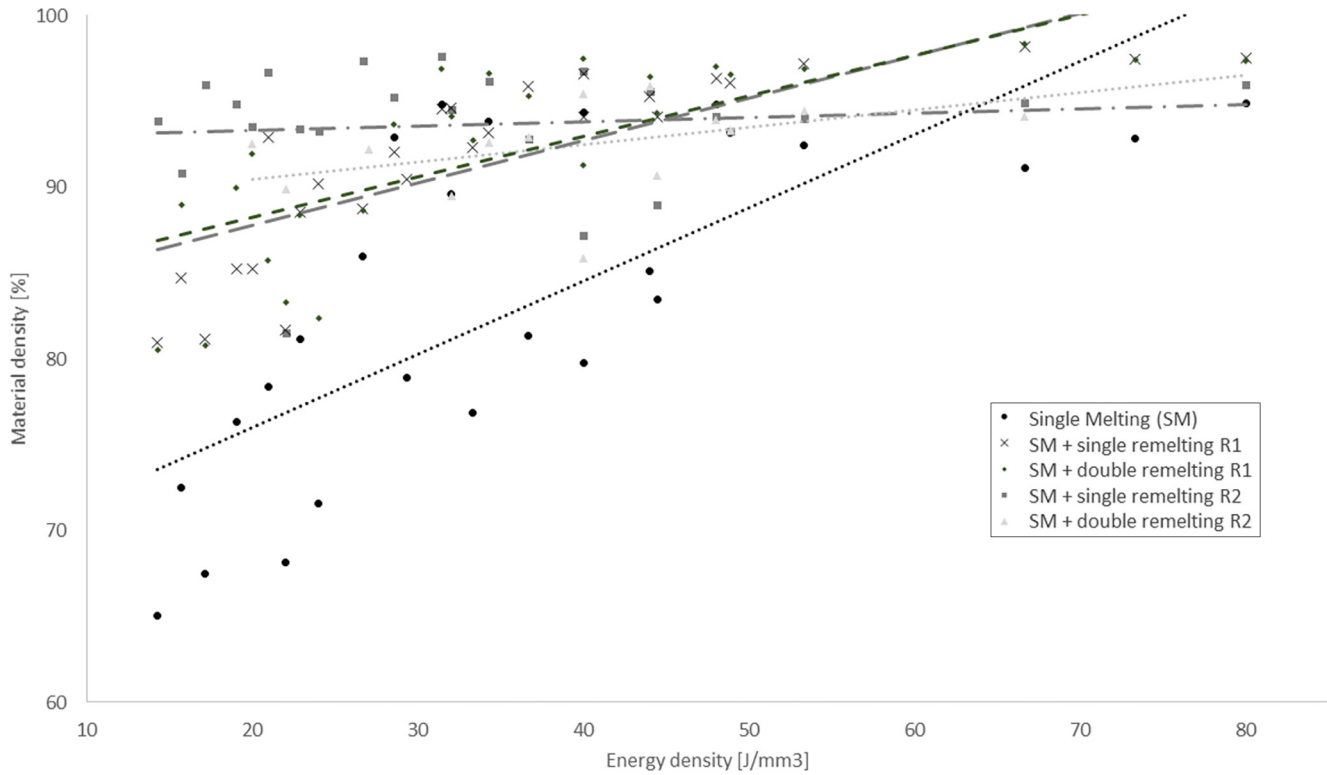

Leuders *et al.* (2013) and Shi *et al.* (2020) have stated that due to the presence of increased thermal gradient, thermal stresses are generated. As a consequence, cracks generated by the thermal stresses increased significantly and led to part failure. The failed parts were excluded from the studies. Since the R2 remelting strategy did not provide good printability results, it was excluded from further investigation.

3.4 Scanning electron microscopy analysis

The chemical composition homogeneity of the parts was further studied with SEM BSE observations and EDS analysis (Figure 7). The intensity of the BSE signal is strongly related to the atomic number (Z) of the specimen. Brighter BSE intensity correlates with greater average Z in the part, and dark areas have a lower average Z. Accordingly, the bright-shaded regions in Figure 7 are Ni-rich, while dark-shaded are Ti-rich. Homogeneity in the presented study is defined as the uniform distribution of Ni and Ti elements in the LPBF-rendered part and is observed as lower phase contrast in BSE images. Chemical composition homogeneity was observed to increase with the number of remelts. To further determine the chemical homogeneity of specimens, EDS measurements were performed. These measurements are shown in Figure 7, where Ni and Ti atoms are more homogeneously distributed in a parts remelted twice, relative to the SM parts. The influence of the SM parameters, especially the value of energy density, on the homogeneity of the parts was examined as well. No significant differences in the homogeneity of parts manufactured with different energy densities in the first melting were observed in a range of 80–20 J/mm^3 for both single melt and remelted parts. It should be noted that inhomogeneity did not disappear completely in any of the remelting processes. That homogeneity increases with increasing energy density was previously described by Zhao *et al.*(2020) and Wang *et al.* (2019). Nevertheless, in abovementioned studies, heat treatment was applied to increase material homogenization and elimination of unwanted phases.

3.5 X-ray diffraction

To identify the phases, XRD analysis was performed on single melt and remelted parts (Figure 8). Multiple phases were identified. This analysis showed that in all parts, regardless of the laser power and amount of remelting, there are NiTi (B2) and (B19'), $NiTi_2$, Ni_4Ti_3 and Ni_3Ti phases. Although, as reported by Halani and Shin (2012) and Wang *et al.* (2019), the peaks of some phases, as NiTi (B19') and Ti_2Ni or NiTi (B2) and Ni_3Ti, overlap each other. The presence of multiple phases is confirmed with the results of the BSE observations and EDS analysis, which revealed high phase contrast and chemical composition differences in the fabricated parts. However, as demonstrated by Zhao *et al.* (2020), high energy densities, above 375 J/mm^3, applied to fabricate elementally blended NiTi, eliminate the presence of Ni_4Ti_3 and Ni_3Ti unwanted secondary phases. Thus, it can be concluded, that lower energy densities, below 80 J/mm^3 and remelting strategies, are not sufficient to blend the elemental components completely and postprocessing heat treatment should be applied.

Figure 7 SEM BSE observations of parts single melt process (a, c) and remelted once (b, e) and twice (c, f) with R1 parameters, EDS maps of parts single melt (g) and remelted twice with R1 parameters (h); red arrows indicate meltpools

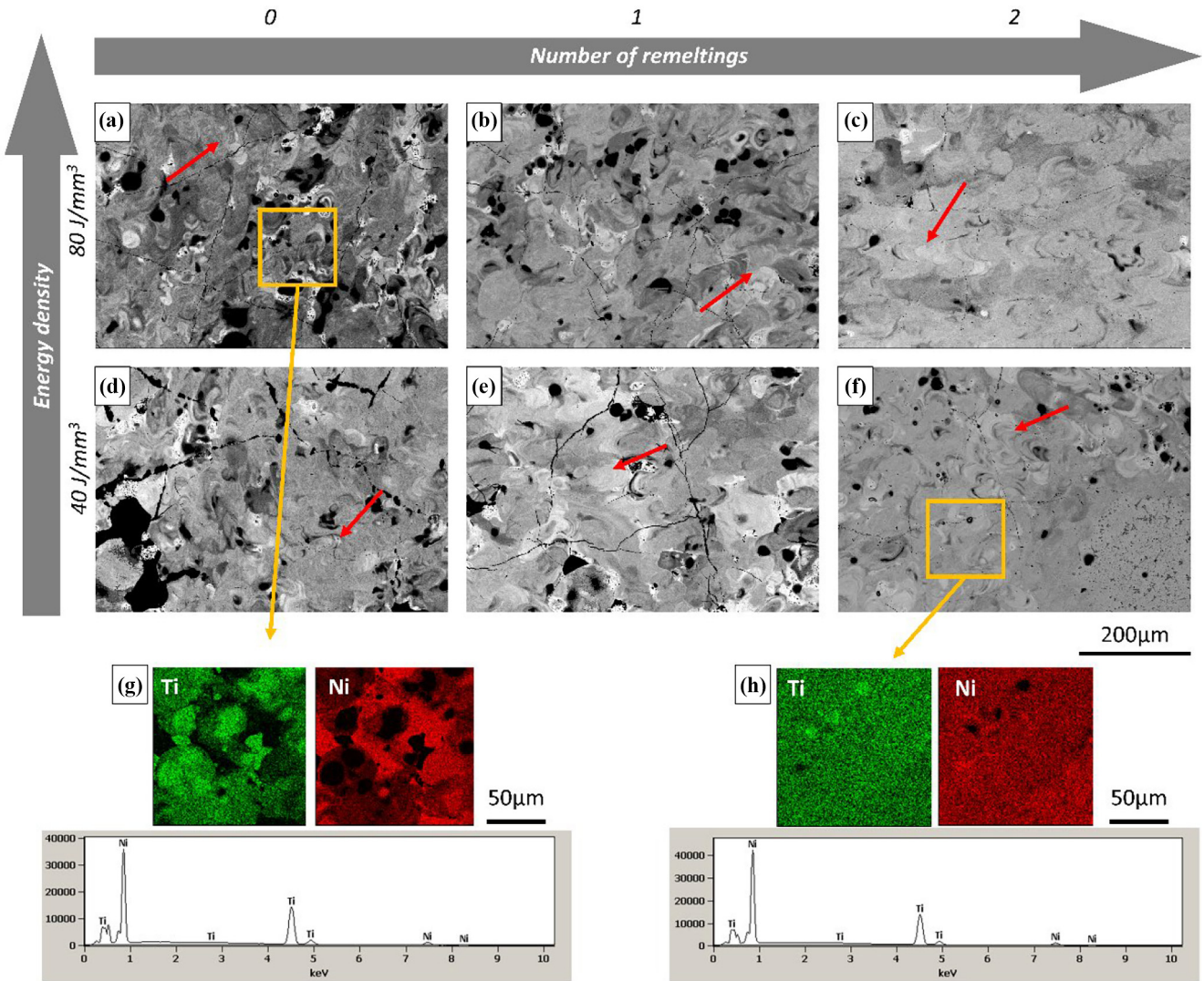

Stress measurement was performed on parts fabricated with SM and R1 single and double remelting. All stress measurements carried out using the diffraction methodology were performed according to the EN-15305 standard and were conducted for the austenitic NiTi phase with cubic structure (space group: Pm-3m) and lattice parameter a_0 = 3.005 Å. The expected penetration depth of Cr radiation into this material was about 20 μm. To realize the analysis of experimental data, a background cutoff was performed, for which the form of a linear function was adopted. The distribution of the diffracted radiation was approximated by a Gaussian function. In the stress analysis, the following values of elasticity constants were assumed: $s_1 = -3.98$ 1/TPa and $\frac{1}{2}s_2 = 16.02$ 1/TPa. The results were calculated to obtain the principal stresses σ_{11} and σ_{22}, their uncertainties $\Delta\sigma_{11}$ and $\Delta\sigma_{22}$ and reduced Huber–von Mises stresses σ_{red} (with uncertainty σ_{red}). The results for these stress measurements are summarized in Table 4.

The results indicate that the lowest stresses are present in SM parts that also have the highest number of cracks and pores (Table 4). Therefore, it can be concluded that the residual stresses generated by the high thermal gradient (i.e. uneven heat deposition and cooling) between melt pool and powder bed have been released at the location of cracks. Likewise, the lowest residual stresses are presented in double melted (SM + single remelting R1) part, which has the lowest number of cracks and pores, indicating that the remelting closed the cracks but did not increase the stress enough to cause further cracks. Furthermore, a third melting run (SM + double remelting R1) resulted in an increased number of cracks. This was likely due to an increase in the heat input generated by the third melt run as well as reduced residual stresses (stresses were released at the site of cracks).

3.6 Microhardness

Figure 9 shows the variation of microhardness for SM and R1 remelted parts. The microhardness of the material presented in this study varied in a range from 487 to 495 HV, depending on implemented number of melts. Furthermore, it can be observed that the measurement error decreases as the number

Figure 8 XRD diffractograms of parts fabricated with SM and R1 single and double remelting

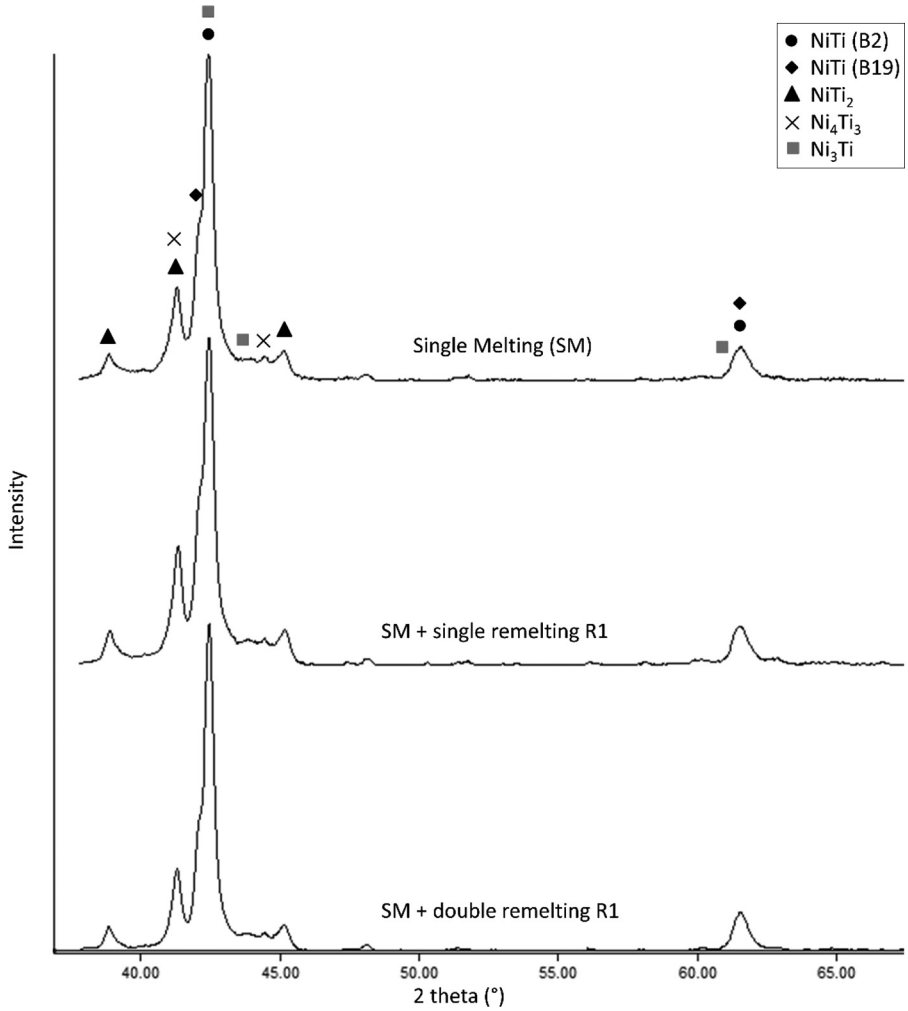

Table 4 XRD stress measurement results of parts fabricated with SM and R1 single and double remelting LPBF

Part no.	σ_{11} [MPa]	$\Delta\sigma_{11}$ [MPa]	σ_{22} [MPa]	$\Delta\sigma_{22}$ [MPa]	σ_{red} [MPa]	$\Delta\sigma_{red}$ [MPa]
Single melting (SM)	50.10	30.85	1.40	35.88	49.41	13.67
SM + single remelting R1	236.7	31.10	214.20	31.10	226.29	30.98
SM + double remelting R1	181.10	57.35	157.70	63.44	170.61	59.34

of remelts increases and is the lowest for parts remelted twice. This may be due to the fact, that SM parts and parts remelted once can have more unmixed regions which are Ni-rich or Ti-rich. This reduction in the measurement error is ascribed to the improvement of microstructure homogeneity. Moreover, microhardness of LPBF-rendered parts using elemental Ni and Ti powders is higher than for LPBF parts rendered from prealloyed NiTi powders as well as conventional fabrication techniques. The average hardness value for the martensite phase of as-cast NiTi, reported by Shishkovsky *et al.* (2012), is 340–440 HV, whereas the average hardness for the Ti_2Ni phase, reported by Zhang *et al.* (2013), is 700 HV. For LPBF-manufactured NiTi, different factors influence the microhardness level, including material composition, powder type (prealloyed or elementally blended), laser parameters and postheat treatment. Moreover, due to the high cooling rates associated with LPBF, high thermal stresses are known to occur. Elahinia *et al.* (2016) have stated that thermal stress enhances microhardness significantly. In case of NiTi alloy manufactured by LPBF from elementally blended powders, the presence of many different phases is an additional factor influencing the hardness.

It was reported by Zhang *et al.* (2013) that parts LPBF-rendered from elementally blended Ni and Ti powders with the composition of $Ni_{55}Ti_{45}$ (which is close to our composition) exhibit microhardness that is dependent on scanning

Figure 9 Microhardness of parts fabricated with SM and R1 single and double remelting

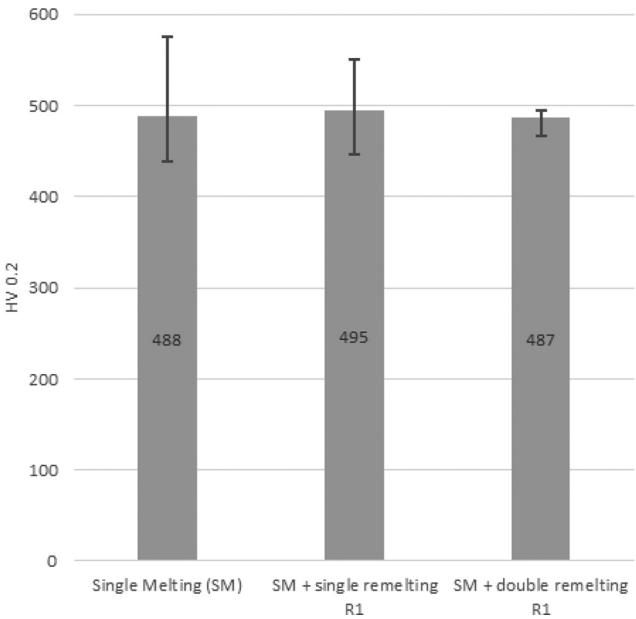

parameters, with the scanning parameters values in their studies varied an average of 360–460 HV. Research presented by Wysocki *et al.* (2017) describes an increase of microhardness that they relate to oxygen pick-up during LPBF fabrication. Kwasniak *et al.* (2016) and Sun *et al.* (2013) claim that oxygen is responsible for solid solution strengthening and, therefore, can enhance the mechanical properties of titanium alloys. The phenomenon of solid solution strengthening of additively manufactured titanium and its alloys was also reported by Wysocki *et al.* (2018, 2017), Velasco-Castro *et al.* (2019) and Pauzon *et al.* (2021).

3.7 Wavelength dispersive X-ray fluorescence chemical composition analysis

Chemical composition of parts fabricated with SM and R1 single and double remelting was analyzed using WD-XRF. The influence of the number of melts on the chemical composition (e.g. nickel evaporation) was studied. The initial content of Ni in batch powder was 55.7 Wt.%. The WD-XRF data showed that the amount of nickel in the material decreases with an increasing number of melt runs (Figure 10). The highest decrease in nickel content was observed after the first melting (1.6 Wt.%), and each subsequent melt run resulted in a smaller reduction in the amount of nickel, which was 0.6 Wt.% and 0.4 Wt.% for the first and second remelting, respectively. The decrease in the amount of evaporated nickel might be due to the fact that pure elements were alloyed after first melting (no peaks of pure Ti and Ni were detected on XRD) and were more thoroughly blended after each melt run, and the evaporation of nickel from NiTi alloy is less than that of pure nickel (Chmielewska *et al.*, 2021). Moreover, the number of melt runs and Ni evaporation can also affect the changes in martensitic and austenitic transformation temperatures of

Figure 10 Chemical composition (Ni content) of parts fabricated with SM and R1 single and double remelting; the measurement error was ±0.33 Wt.%

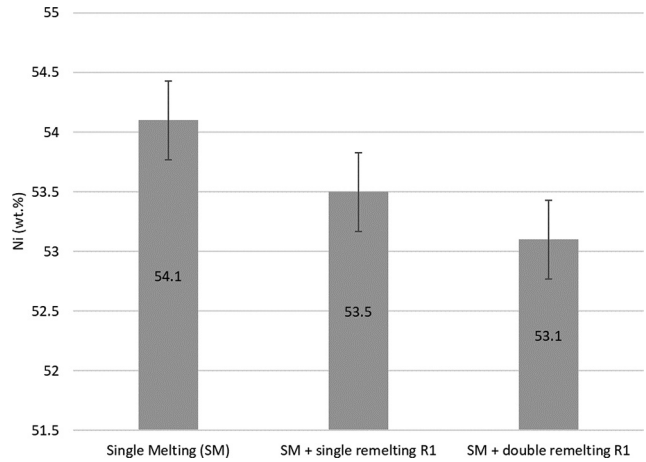

NiTi. These differences were described by Chmielewska *et al.* (2021).

3.8 Oxygen content analysis

An oxygen content study was performed to determine whether the number of melt runs influences oxygen pick-up. An average presence of 0.54 Wt.% of the oxygen is observed across all parts in our study (Table 5). The oxygen level in the building chamber during the fabrication process was below 0.3 Vol.%. Additionally, the elemental nickel powder is claimed to be free of oxygen by the vendor (Table 1), and titanium elemental powders contain <0.18% of the oxygen (Table 2). Therefore, it can be concluded that oxygen that was introduced into the parts during the first melt run, and subsequent melt runs did not influence the oxygen level in the material.

3.9 μCT and Archimedes density measurement

The density of parts fabricated with single melt and R1 single and double remelting was evaluated by Archimedes density measurement (Figure 11) and μCT (Figure 12). To provide high quality of μCT scans, a section of 3 × 3 × 3 mm of each part was analyzed. Archimedes density measurement showed that parts fabricated with SM, R1 single, and S1 double remelting had a density of 95.88, 98.70 and 99.02%, respectively, versus the theoretical value for NiTi alloy. The calculated density based on μCT for these same three study groups was 94.95, 98.33 and 99.17%, respectively. Moreover, μCT results showed that pores present in the parts are irregularly shaped. The densities measured with both methods did not significantly differ from each other (differences were below 0.93%). Both analyses showed that remelting improves

Table 5 Oxygen content in parts fabricated with SM and R1 single and double remelting; the measurement error was ±0.1 Wt.%

	Single melting (SM)	SM + single remelting R1	SM + double remelting R1
Oxygen content (Wt.%)	0.54	0.54	0.54

Figure 11 Archimedes density measurement of parts fabricated with SM and R1 single and double remelting

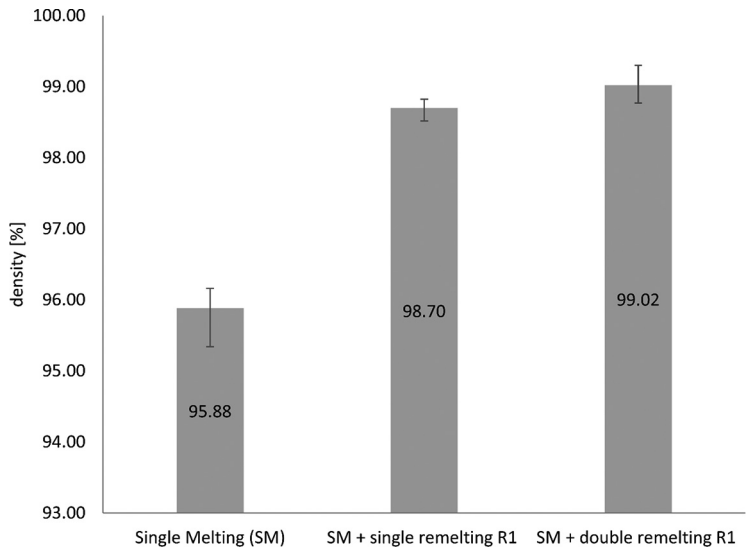

Figure 12 Density analyses of μCT-scans of sample parts fabricated with SM and R1 single and double remelting

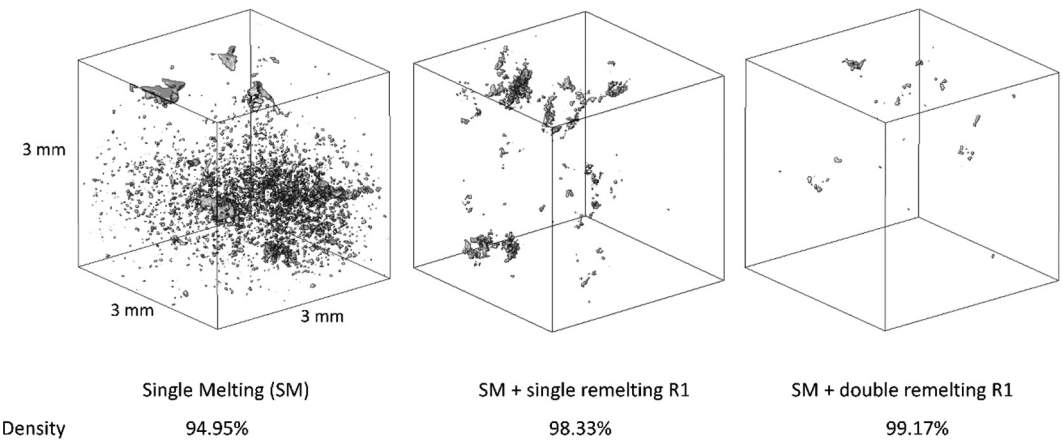

the density of parts fabricated from elemental Ni and Ti powders and that the density increases with an increasing number of melt runs.

4. Conclusions

For the first time, Ni and Ti elementally blended powders were used to fabricate NiTi parts via LPBF using remelting strategies. The influence of the number of remelts, with the same energy density (J/mm^3) but obtained with different laser process parameters (i.e. laser power, scanning speed), on final NiTi part homogeneity was studied. The study showed that using remelting parameters with the same value of the energy density but resulting from different values of laser power (25 and 75 W) and scanning speed (1,000 and 3,000 mm/s) give radically different results. Remelting was observed to significantly reduce porosity. The relatively high density, revealed with μCT reconstruction estimated at the value at 99.17%, was observed for parts where remelting was applied. Additionally, remelting R1, with lower laser power and scanning speed, eliminated cracks, while remelting R2, with higher laser power and scanning speed, generated a high thermal gradient that is expected to promote the formation and growth of cracks. Increased NiTi homogeneity was observed to correlate with the increasing number of remelts. However, multiple phases were observed regardless of the number of remelts; thus, postprocessing heat treatment should be investigated in future research on LPBF remelting of Ni and Ti elemental powders. The microhardness of the parts remelted twice was more uniform than parts produced from a single melt or remelted once. XRD stress measurement suggested that residual stress and crack occurrence was reduced in LPBF processes that include remelting. WD-XRF chemical composition analysis showed that the highest amount of Ni evaporated during first melt run (SM) and subsequent melt runs did not influence Ni evaporation significantly. In conclusion, remelting was observed to significantly improve

the blending of the Ni and Ti elemental powders during LPBF compared with single melt processes; however, it did not eliminate phase composition inhomogeneity entirely.

References

Ali, H., Ma, L., Ghadbeigi, H. and Mumtaz, K. (2017), "In-situ residual stress reduction, martensitic decomposition and mechanical properties enhancement through high temperature powder bed pre-heating of selective laser melted Ti6Al4V", *Materials Science and Engineering: A*, Vol. 695, pp. 211-220.

Bandyopadhyay, A. and Bose, S. (2015), *Additive Manufacturing*, in Bandyopadhyay, A. and Bose, S. (Eds), 1st ed., CRC Press Taylor & Francis Group, Boca Raton, doi: 10.1201/b18893.

Chen, K.C. (2003), "NiTi – magic or phase transformations?", *ASEE Annual Conference Proceedings*, pp. 2423-2430.

Chen, H., Gu, D., Dai, D., Xia, M. and Ma, C. (2018), "A novel approach to direct preparation of complete lath martensite microstructure in tool steel by selective laser melting", *Materials Letters*, Vol. 227, pp. 128-131.

Chen, X., Liu, K., Guo, W., Gangil, N., Siddiquee, A.N. and Konovalov, S. (2019), "The fabrication of NiTi shape memory alloy by selective laser melting: a review", *Rapid Prototyping Journal*, Vol. 25 No. 8, pp. 1421-1432.

Chmielewska, A., Wysocki, B., Żrodowski, Ł. and Święszkowski, W. (2019), "Hybrid solid-porous titanium scaffolds", *Transactions on Additive Manufacturing Meets Medicine*, Infinite Science Publishing, Lubeck, Germany, Vol. 1, p. 2.

Chmielewska, A., Wysocki, B., Buhagiar, J., Michalski, B., Adamczyk-Cieślak, B., Gloc, M. and Święszkowski, W. (2021), "In situ alloying of NiTi: influence of laser powder bed fusion (LBPF) scanning strategy on chemical composition", *Materials Today Communications*, Vol. 30, p. 103007.

Dadbakhsh, S., Speirs, M., Kruth, J.P., Schrooten, J., Luyten, J. and Van Humbeeck, J. (2014), "Effect of SLM parameters on transformation temperatures of shape memory nickel titanium parts", *Advanced Engineering Materials*, Vol. 16 No. 9, pp. 1140-1146.

Dhanasekaran, R., Reddy, S.S., Kumar, B.G. and Anirudh, A.S. (2018), "Shape memory materials for bio-medical and aerospace applications", *Materials Today: Proceedings*, Vol. 5 No. 10, pp. 21427-21435.

Dong, D., Chang, C., Wang, H., Yan, X., Ma, W., Liu, M., Deng, S., Gardan, J., Bolot, R. and Liao, H. (2021), "Selective laser melting (SLM) of CX stainless steel: theoretical calculation, process optimization and strengthening mechanism", *Journal of Materials Science & Technology*, Vol. 73, pp. 151-164.

Duerig, T., Pelton, A. and Sto, D. (1999), "An overview of nitinol medical applications", *Materials Science and Engineering: A*, Vols 273/275, pp. 149-160.

Elahinia, M.H., Hashemi, M., Tabesh, M. and Bhaduri, S.B. (2012), "Manufacturing and processing of NiTi implants: a review", *Progress in Materials Science*, Vol. 57 No. 5, pp. 911-946.

Elahinia, M., Shayesteh Moghaddam, N., Taheri Andani, M., Amerinatanzi, A., Bimber, B.A. and Hamilton, R.F. (2016), "Fabrication of NiTi through additive manufacturing: a review", *Progress in Materials Science*, Vol. 83, pp. 630-663.

Farber, E., Zhu, J.N., Popovich, A. and Popovich, V. (2019), "A review of NiTi shape memory alloy as a smart material produced by additive manufacturing", *Materials Today: Proceedings*, Vol. 30, pp. 761-767.

Fischer, M., Joguet, D., Robin, G., Peltier, L. and Laheurte, P. (2016), "In situ elaboration of a binary Ti-26Nb alloy by selective laser melting of elemental titanium and niobium mixed powders", *Materials Science and Engineering: C*, Vol. 62, pp. 852-859.

Frenzel, J., George, E.P., Dlouhy, A., Somsen, C., Wagner, M.F.X. and Eggeler, G. (2010), "Influence of Ni on martensitic phase transformations in NiTi shape memory alloys", *Acta Materialia, Acta Materialia Inc*, Vol. 58 No. 9, pp. 3444-3458.

Gibson, I., Rosen, D. and Stucker, B. (2015), *Additive Manufacturing Technologies 3D Printing, Rapid Prototyping, and Direct Digital Manufacturing*, 2nd ed., Springer, Berlin, doi: 10.2495/SDP-V9-N5-658-668.

Griffiths, S., Rossell, M.D., Croteau, J., Vo, N.Q., Dunand, D.C. and Leinenbach, C. (2018), "Effect of laser rescanning on the grain microstructure of a selective laser melted Al-Mg-Zr alloy", *Materials Characterization*, Vol. 143, pp. 34-42.

Guo, M., Gu, D., Xi, L., Du, L., Zhang, H. and Zhang, J. (2019), "Formation of scanning tracks during selective laser melting (SLM) of pure tungsten powder: morphology, geometric features and forming mechanisms", *International Journal of Refractory Metals and Hard Materials*, Vol. 79, pp. 37-46.

Halani, P.R. and Shin, Y.C. (2012), "In situ synthesis and characterization of shape memory alloy nitinol by laser direct deposition", *Metallurgical and Materials Transactions A*, Vol. 43 No. 2, pp. 650-657.

Humbeeck, J.V. (1999), "Non-medical applications of shape memory alloys", *Materials Science and Engineering A*, Vol. 273, pp. 134-148.

Khalil-Allafi, J. and Amin-Ahmadi, B. (2009), "The effect of chemical composition on enthalpy and entropy changes of martensitic transformations in binary NiTi shape memory alloys", *Journal of Alloys and Compounds*, Vol. 487 Nos 1/2, pp. 363-366.

Kwasniak, P., Garbacz, H. and Kurzydlowski, K.J. (2016), "Solid solution strengthening of hexagonal titanium alloys: restoring forces and stacking faults calculated from first principles", *Acta Materialia*, Vol. 102, pp. 304-314.

Leuders, S., Thöne, M., Riemer, A., Niendorf, T., Tröster, T., Richard, H.A. and Maier, H.J. (2013), "On the mechanical behaviour of titanium alloy TiAl6V4 manufactured by selective laser melting: fatigue resistance and crack growth performance", *International Journal of Fatigue*, Vol. 48, pp. 300-307.

Li, B.Q., Li, Z. and Liu, B. (2019), "Selective laser remelting of an additive layer manufacturing process on AlSi10Mg", *Results in Physics*, Vol. 12, pp. 982-988.

Li, R., Liu, J., Shi, Y., Wang, L. and Jiang, W. (2012), "Balling behavior of stainless steel and nickel powder during selective laser melting process", *The International Journal of Advanced Manufacturing Technology*, Vol. 59 Nos 9/12, pp. 1025-1035.

Liu, B., Fang, G. and Lei, L. (2021), "An analytical model for rapid predicting molten Pool geometry of selective laser melting (SLM)", *Applied Mathematical Modelling*, Vol. 92, pp. 505-524.

Liu, S. and Guo, H. (2020), "Balling behavior of selective laser melting (SLM) magnesium alloy", *Materials*, Vol. 13 No. 16, p. 3632, doi: 10.3390/MA13163632.

Lu, P., Cheng-Lin, Z., Hai-Yi, L., Liang, W. and Tong, L. (2020), "A new two-step selective laser remelting of 316L stainless steel: process, density, surface roughness, mechanical properties, microstructure", *Materials Research Express*, Vol. 7 No. 5, p. 56503, doi: 10.1088/2053-1591/ab8b86.

Motemani, Y., Nili-Ahmadabadi, M., Tan, M.J., Bornapour, M. and Rayagan, S. (2009), "Effect of cooling rate on the phase transformation behavior and mechanical properties of Ni-rich NiTi shape memory alloy", *Journal of Alloys and Compounds*, Vol. 469 Nos 1/2, pp. 164-168.

Pauzon, C., Dietrich, K., Forêt, P., Hryha, E. and Witt, G. (2021), "Mitigating oxygen pick-up during laser powder bed fusion of Ti-6Al-4V by limiting heat accumulation", *Materials Letters*, The Author(s), Vol. 288, p. 129365.

Sato, Y., Tsukamoto, M., Shobu, T., Yamashita, Y., Yamagata, S., Higashino, R., Masuno, S., Higashino, R., Nishi, T., Yamashita, Y., Nakano, H. and Abe, N. (2017), "Effect of baseplate temperature on sputter-generation for development of SLM in vacuum", *Lasers in Manufacturing Conference*, p. 4.

Sharma, K. and Srinivas, G. (2019), "Flying smart: smart materials used in aviation industry", *Materials Today: Proceedings*, doi: 10.1016/j.matpr.2019.10.115.

Shi, X., Wang, H., Feng, W., Zhang, Y., Ma, S. and Wei, J. (2020), "The crack and pore formation mechanism of Ti–47Al–2Cr–2Nb alloy fabricated by selective laser melting", *International Journal of Refractory Metals and Hard Materials*, Vol. 91, p. 105247.

Shishkovsky, I., Yadroitsev, I. and Smurov, I. (2012), "Direct selective laser melting of nitinol powder", *Physics Procedia*, Vol. 39, pp. 447-454.

Simonelli, M., Aboulkhair, N.T., Cohen, P., Murray, J.W., Clare, A.T., Tuck, C. and Hague, R.J.M. (2018), "A comparison of Ti-6Al-4V in-situ alloying in selective laser melting using simply-mixed and satellited powder blend feedstocks", *Materials Characterization*, Vol. 143, pp. 118-126.

Stoll, P., Spierings, A. and Wegner, K. (2020), "SLM processing of elementally blended NiTi shape memory alloy", *Procedia CIRP*, Vol. 95, pp. 121-126.

Sun, B., Li, S., Imai, H., Mimoto, T., Umeda, J. and Kondoh, K. (2013), "Fabrication of high-strength Ti materials by in-process solid solution strengthening of oxygen via P/M methods", *Materials Science and Engineering: A*, Vol. 563, pp. 95-100.

Tang, X., Zhang, S., Zhang, C., Chen, J., Zhang, J. and Liu, Y. (2020), "Optimization of laser energy density and scanning strategy on the forming quality of 24CrNiMo low alloy steel manufactured by SLM", *Materials Characterization*, Vol. 170, p. 110718.

Thomas, F. (2015), "The effect of various quenchants on the hardness and microstructure of 60-NITINOL", Nasa/TM-2015-218463.

Trapp, J., Rubenchik, A.M., Guss, G. and Matthews, M.J. (2017), "In situ absorptivity measurements of metallic powders during laser powder-bed fusion additive manufacturing", *Applied Materials Today*, Vol. 9, pp. 341-349.

Velasco-Castro, M., Hernández-Nava, E., Figueroa, I.A., Todd, I. and Goodall, R. (2019), "The effect of oxygen pickup during selective laser melting on the microstructure and mechanical properties of Ti–6Al–4V lattices", *Heliyon*, Vol. 5 No. 12, p. e02813.

Vrancken, B., Thijs, L., Kruth, J.P. and Van Humbeeck, J. (2014), "Microstructure and mechanical properties of a novel β titanium metallic composite by selective laser melting", *Acta Materialia, Acta Materialia Inc*, Vol. 68, pp. 150-158.

Wang, C., Tan, X.P., Du, Z., Chandra, S., Sun, Z., Lim, C.W.J., Tor, S.B., Lim, C.S. and Wong, C.H. (2019), "Additive manufacturing of NiTi shape memory alloys using pre-mixed powders", *Journal of Materials Processing Technology*, Vol. 271, pp. 152-161.

Wang, Z., Wang, X., Zhou, X., Ye, G., Cheng, X., Cheng, X. and Zhang, P. (2020), "Investigation into spatter particles and their effect on the formation quality during selective laser melting processes", *Computer Modeling in Engineering & Sciences*, Vol. 124 No. 1, pp. 243-263.

Wei, K., Lv, M., Zeng, X., Xiao, Z., Huang, G., Liu, M. and Deng, J. (2019), "Effect of laser remelting on deposition quality, residual stress, microstructure, and mechanical property of selective laser melting processed Ti-5Al-2.5Sn alloy", *Materials Characterization*, Vol. 150, pp. 67-77.

Wejrzanowski, T., Lewandowska, M. and Kurzydłowski, K.J. (2010), "Stereology of nano-materials", *Image Analysis & Stereology*, Vol. 29 No. 1, pp. 1-12.

Wejrzanowski, T., Spychalski, W.L., Rózniatowski, K. and Kurzydłowski, K.J. (2008), "Image based analysis of complex microstructures of engineering materials", *International Journal of Applied Mathematics and Computer Science*, Vol. 18 No. 1, pp. 33-39.

Weller, C., Kleer, R. and Piller, F. (2015), "Economic implications of 3D printing: market structure models in light of additive manufacturing revisited", *International Journal of Production Economics*, Vol. 164, pp. 43-56, doi: 10.1016/j.ijpe.2015.02.020.

Wysocki, B., Idaszek, J., Zdunek, J., Rozniatowski, K., Pisarek, M., Yamamoto, A. and Swieszkowski, W. (2018), "The influence of selective laser melting (SLM) process parameters on In-Vitro cell response", *International Journal of Molecular Sciences*, Vol. 19 No. 6, p. 1619, doi: 10.3390/ijms19061619.

Wysocki, B., Maj, P., Krawczyńska, A., Rożniatowski, K., Zdunek, J., Kurzydłowski, K.J. and Święszkowski, W. (2017), "Microstructure and mechanical properties investigation of CP titanium processed by selective laser melting (SLM)", *Journal of Materials Processing Technology*, Vol. 241, pp. 13-23.

Xiong, Z., Zhang, P., Tan, C., Dong, D., Ma, W. and Yu, K. (2020), "Selective laser melting and remelting of pure tungsten", *Advanced Engineering Materials*, Vol. 22 No. 3, pp. 1-9.

Zhang, B., Chen, J. and Coddet, C. (2013), "Microstructure and transformation behavior of in-situ shape memory alloys by selective laser melting Ti-Ni mixed powder", *Journal of Materials Science & Technology*, Vol. 29 No. 9, pp. 863-867.

Zhang, H., Zhao, Y., Huang, S., Zhu, S., Wang, F. and Li, D. (2019), "Manufacturing and analysis of high-performance refractory high-entropy alloy via selective laser melting (SLM)", *Materials*, Vol. 12 No. 5, p. -720, doi: 10.3390/ma12050720.

Zhao, C., Liang, H., Luo, S., Yang, J. and Wang, Z. (2020), "The effect of energy input on reaction, phase transition and shape memory effect of NiTi alloy by selective laser melting", *Journal of Alloys and Compounds*, Vol. 817, p. 153288.

Further reading

Andani, M.T., Shayesteh Moghaddam, N., Haberland, C., Dean, D., Miller, M.J. and Elahinia, M. (2014), "Metals for bone implants. Part 1. powder metallurgy and implant rendering", *Acta biomaterialia, Acta Materialia Inc.*, Vol. 10, Vol. 10 No. 10, pp. 4058-4070.

Arun, I.D., Chakravarthy, P., Arockiakumar, R. and Santhosh, B. (2018), *Shape Memory Materials*, 1st ed., CRC Press Taylor & Francis Group, Boca Raton, doi: 10.1201/9781351119948.

Gong, H., Rafi, K., Gu, H., Janaki Ram, G.D., Starr, T. and Stucker, B. (2015), "Influence of defects on mechanical properties of Ti-6Al-4V components produced by selective laser melting and electron beam melting", *Materials & Design*, Vol. 86, pp. 545-554.

Hodgson, D.E., Wu, M.H. and Biermann, R.J. (2013), *Shape Memory Alloys, ASM Handbook*, Vol. 2, ASM International, Novelty, OH, doi: 10.1017/cbo9781139025164.004.

Khoo, Z.X., Liu, Y., An, J., Chua, C.K., Shen, Y.F. and Kuo, C.N. (2018), "A review of selective laser melted NiTi shape memory alloy", *Materials*, Vol. 11 No. 4, pp. 11-17.

Memry Corporation (2017), *Introduction to Nitinol*, Memry Corporation, Bethel, CT.

Miyazaki, S., Kim, H.Y. and Hosoda, H. (2006), "Development and characterization of Ni-free Ti-base shape memory and superelastic alloys", *Materials Science and Engineering: A*", Vol. 438-440, pp. 18-24.

Ou, S.-F., Peng, B.-Y., Chen, Y.-C. and Tsai, M.-H. (2018), "Manufacturing and characterization of NiTi alloy with functional properties by selective laser melting", *Metals*, Vol. 8 No. 5, pp. 342.

Patil, A.N. and Sarje, S.H. (2021), "Additive manufacturing with shape changing/memory materials: a review on 4D printing technology", *Materials Today: Proceedings*, Vol. 44 No. 40, pp. 11-16.

Shabalovskaya, S., Anderegg, J. and Van Humbeeck, J. (2008), "Critical overview of nitinol surfaces and their modifications for medical applications", *Acta Biomaterialia*, Vol. 4 No. 3, pp. 447-467.

Speirs, M., Wang, X., Van Baelen, S., Ahadi, A., Dadbakhsh, S., Kruth, J.-P. and Van Humbeeck, J. (2016), "On the transformation behavior of NiTi Shape-Memory alloy produced by SLM", *Shape Memory and Superelasticity*, Vol. 2 No. 4, pp. 310-316.

Sun, K., Peng, W., Yang, L. and Fang, L. (2020), "Effect of SLM processing parameters on microstructures and mechanical properties of al0.5 CoCrFeNi high entropy alloys", *Metals*, Vol. 10 No. 2, p. 292, doi: 10.3390/met10020292.

Wegener, K., Spierings, A. and Staub, A. (2020), "Bioinspired intelligent SLM cell", *Procedia CIRP*, Vol. 88, pp. 624-629.

Appendix 1. Optimization procedure and optimization parameters

The optimization procedure was performed by fabrication of the samples with five sets of process parameters stated in Tables A1–A9. The first set of process parameters shown in Table A1 was based on the process parameters used for processing of the prealloyed NiTi powder.

Parameters no. 1

In the first set of the parameters, SM of each layer was performed with a wide range of energy densities (17–198 J/mm^3), and low laser powers in a range of 32.5 W–42.5 W. The low laser powers are, in our experience, beneficial for the defect free fabrication of the titanium alloys that was described in our previous study (Chmielewska *et al.*, 2021). While a few parameters form the set of Parameters no. 1 (energy densities lower than 70 J/mm^3) allowed for the fabrication of samples with acceptable quality (Figure A1), majority of them (fabricated with energy densities higher than 70 J/mm^3) were failed due to the overheating and excessive melting. The dark overheated samples visible on the Realizer SLM50 building platform are shown in Figure A1. The microstructure of representative samples fabricated with some

Table A1 Parameters no. 1 (single melting – SM)

No.	*t* [mm]	h [μm]	pd [μm]	ext [μs]	v [mm/s]	P [W]	E [J/mm^3]
1	25	120	10	20	500	32.5	22
2	25	120	10	40	250	32.5	43
3	25	120	10	60	167	32.5	65
4	25	120	10	80	125	32.5	87
5	25	120	10	100	100	32.5	108
6	25	120	10	120	83	32.5	130
7	25	120	10	140	71	32.5	152
8	25	150	10	20	500	32.5	17
9	25	150	10	40	250	32.5	35
10	25	150	10	60	167	32.5	52
11	25	150	10	80	125	32.5	69
12	25	150	10	100	100	32.5	87
13	25	150	10	120	83	32.5	104
14	25	150	10	140	71	32.5	121
15	25	120	10	20	500	42.5	23
16	25	120	10	40	250	42.5	45
17	25	120	10	60	167	42.5	85
18	25	120	10	80	125	42.5	113
19	25	120	10	100	100	42.5	142
20	25	120	10	120	83	42.5	170
21	25	120	10	140	71	42.5	198
22	25	150	10	20	500	42.5	28
23	25	150	10	40	250	42.5	57
24	25	150	10	60	167	42.5	85
25	25	150	10	80	125	42.5	91
26	25	150	10	100	100	42.5	113
27	25	150	10	120	83	42.5	136
28	25	150	10	140	71	42.5	159

Table A2 Parameters no. 2 (scanning strategies 2.1–2.5)

No.	*t* [mm]	h [μm]	pd [μm]	ext [μs]	v [mm/s]	lp [W]	E[J/mm^3]
1	25	120	20	20	1,000	27.5	9
2	25	120	20	40	500	27.5	18
3	25	120	20	60	333	27.5	28
4	25	120	20	80	250	27.5	37
5	25	120	20	100	200	27.5	46
6	25	120	20	120	167	27.5	55
7	25	120	20	140	143	27.5	64
8	25	150	20	20	1,000	27.5	7
9	25	150	20	40	500	27.5	15
10	25	150	20	60	333	27.5	22
11	25	150	20	80	250	27.5	29
12	25	150	20	100	200	27.5	37
13	25	150	20	120	167	27.5	44
14	25	150	20	140	143	27.5	51
15	25	120	20	20	1,000	37.5	13
16	25	120	20	40	500	37.5	25
17	25	120	20	60	333	37.5	38
18	25	120	20	80	250	37.5	50
19	25	120	20	100	200	37.5	63
20	25	120	20	120	167	37.5	75
21	25	120	20	140	143	37.5	88
22	25	150	20	20	1,000	37.5	10
23	25	150	20	40	500	37.5	20
24	25	150	20	60	333	37.5	30
25	25	150	20	80	250	37.5	40
26	25	150	20	100	200	37.5	50
27	25	150	20	120	167	37.5	60
28	25	150	20	140	143	37.5	70

Table A3 Additional melting (remelting) applied to parameters no. 2 (scanning strategies 2.3–2.5)

No.	*t* [mm]	h [μm]	pd [μm]	ext [μs]	v [mm/s]	P [W]	E[J/mm^3]
(P/R)	25	150	10	20	500	27.5	15

of Parameters no. 1 (1, 5, 8, 12) are shown in Figure A2. Based on the obtained results, modification of the Parameters no. 1 was implemented and new set of parameters (Parameters no. 2) was determined.

Based on the obtained results, modification of the Parameters no. 1 were implemented.

Parameters no. 2

The results of samples fabricated with Parameters 1 showed that the best quality was obtained for samples fabricated with energy densities below 70 J/mm^2. Thus, the parameters from the first set of parameters (Table A1) were modified by decreasing laser power and increasing point distance to use energy densities lower than 70 J/mm^3 (Table A2). All single melted samples with parameters 2.1. (single melting) were successfully fabricated; however, the porosity of these samples was significant, so we have decided to add additional process variations to decrease porosity (additional meltings with rotation within successive melt runs). These process variations (scanning strategies) are sets numbered 2.2–2.5.

Table A4 Parameters no. 3 (scanning strategies 3.1–3.6)

No.	*t* [mm]	h [μm]	pd [μm]	ext [μs]	v [mm/s]	P [W]	E [J/mm^3]
1	25	50	10	20	500	37.5	60
2	25	50	20	20	1,000	37.5	30
3	25	50	10	20	500	32.5	52
4	25	50	20	20	1,000	32.5	26
5	25	50	10	20	500	27.5	44
6	25	50	20	20	1,000	27.5	22
7	25	100	10	20	500	37.5	30
8	25	100	20	20	1,000	37.5	15
9	25	100	10	20	500	32.5	26
10	25	100	20	20	1,000	32.5	13
11	25	100	10	20	500	27.5	22
12	25	100	20	20	1,000	27.5	11
13	25	120	10	20	500	37.5	25
14	25	120	20	20	1,000	37.5	13
15	25	120	10	20	500	32.5	22
16	25	120	20	20	1,000	32.5	11
17	25	120	10	20	500	27.5	18
18	25	120	20	20	1,000	27.5	9
19	25	150	10	20	500	37.5	20
20	25	150	20	20	1,000	37.5	10
21	25	150	10	20	500	32.5	17
22	25	150	20	20	1,000	32.5	9
23	25	150	10	20	500	27.5	15
24	25	150	20	20	1,000	27.5	7

Table A5 Additional melting (remelting) applied to parameters no. 3 (scanning strategies 3.3–3.7)

No.	*t* [mm]	h [μm]	pd [μm]	ext [μs]	v [mm/s]	P [W]	E[J/mm^3]
(P/R)	25	150	10	20	500	27.5	15

List of the variations (scanning strategies) for Parameters no. 2:

2.1. SM.
2.2. Double melting: 2x single melting (45° rotation).
2.3. Double melting: premelting (P/R) and single melting (45° rotation).
2.4. Double melting: single melting and remelting (P/R) (45° rotation).
2.5. Double melting: single melting and remelting (P/R) (no rotation).

First variation of the process Parameters 2.1 was adding additional scanning with the same process parameters. The double melting with Parameters no. 2 is double melting with parameters of single melting (45 rotation) which is noted as Parameters 2.2. The macroscopic observation showed that Parameters 2.2 caused overheating for the majority of the samples, while microscopic observations of samples made with Parameters 2.2 showed an increase in porosity compared to single melted (2.1) samples. Majority of the samples failed in the early stage of fabrication. Thus, for the next set of samples (Parameters 2.3–2.5), additional scanning with lower energy density was applied. For samples 2.2–2.4, the rotation of 45° between first and subsequent melt run was applied. The

Table A6 Parameters no. 4 (scanning strategies 4.1–4.7)

No.	*t* [mm]	h [μm]	pd [μm]	ext [μs]	v [mm/s]	P [W]	E [J/mm^3]
1	25	30	10	20	500	30	80
2	25	30	15	20	750	30	53
3	25	30	20	20	1,000	30	40
4	25	30	10	20	500	27.5	73
5	25	30	15	20	750	27.5	49
6	25	30	20	20	1,000	27.5	37
7	25	30	10	20	500	25	67
8	25	30	15	20	750	25	44
9	25	30	20	20	1,000	25	33
10	25	70	10	20	500	30	34
11	25	70	15	20	750	30	23
12	25	70	20	20	1,000	30	17
13	25	70	10	20	500	27.5	31
14	25	70	15	20	750	27.5	21
15	25	70	20	20	1,000	27.5	16
16	25	70	10	20	500	25	29
17	25	70	15	20	750	25	19
18	25	70	20	20	1,000	25	14
19	25	100	10	20	500	42.5	34
20	25	100	15	20	750	42.5	23
21	25	100	20	20	1,000	42.5	17
22	25	100	10	20	500	47.5	38
23	25	100	15	20	750	47.5	25
24	25	100	20	20	1,000	47.5	19

Table A7 Additional melting (remelting) applied to parameters no. 4 (scanning strategies 4.2–4.7)

No.	*t* [mm]	h [μm]	pd [μm]	ext [μs]	v [mm/s]	P [W]	E [J/mm^3]
R_a	25	150	20	20	1,000	25	6.7
R_b	25	150	20	20	1,000	75	20.0

results showed that after producing only a few layers, the surface roughness was very high, and the side cracks presented on some samples caused them to wrap and detach from the substrate. Thus, further production was not possible due to the risk of wiper(coater) damage. Only a few samples were successfully fabricated; however, they possessed high porosity (Figure A4). We have observed the phenomena of welding contamination collection described in the manuscript (Section 3.2; Figure A3). Thus, for the 2.5 set of parameters, no rotation was applied. It allowed for successful fabrication of majority of the samples and porosity decrease compared to single melted (2.1) samples. Based on this observation, we decided not to apply rotation in further study.

Fabricated samples on the platforms along with platforms numbers and the marking of samples on the platforms are presented in Figure A3.

Metallographic observations of polished samples were performed (Figure A4). Nevertheless, due to the high porosity and delamination, some of the samples could not be removed from the platform in a form that allows the preparation of metallographic samples (samples were damaged when removed from the building platform). The samples that could not be successfully removed from the platform were eliminated from further analysis. Moreover, the samples that failed in the early stage of fabrication (after few layers) were not analyzed.

Table A8 Parameters no. 5 (scanning strategies 5.1–5.6)

No.	*t* [mm]	h [μm]	pd [μm]	ext [μs]	v [mm/s]	P [W]	E [J/mm^3]
1	25	30	10	20	500	30	80
2	25	30	15	20	750	30	53
3	25	30	20	20	1,000	30	40
4	25	30	10	20	500	27.5	73
5	25	30	15	20	750	27.5	49
6	25	30	20	20	1,000	27.5	37
7	25	30	10	20	500	25	67
8	25	30	15	20	750	25	44
9	25	30	20	20	1,000	25	33
10	25	50	10	20	500	30	48
11	25	50	15	20	750	30	32
12	25	50	20	20	1,000	30	24
13	25	50	10	20	500	27.5	44
14	25	50	15	20	750	27.5	29
15	25	50	20	20	1,000	27.5	22
16	25	50	10	20	500	25	40
17	25	50	15	20	750	25	27
18	25	50	20	20	1,000	25	20
19	25	70	10	20	500	30	34
20	25	70	15	20	750	30	23
21	25	70	20	20	1,000	30	17
22	25	70	10	20	500	27.5	31
23	25	70	15	20	750	27.5	21
24	25	70	20	20	1,000	27.5	16
25	25	70	10	20	500	25	29
26	25	70	15	20	750	25	19
27	25	70	20	20	1,000	25	14

Table A9 Additional melting (remelting) applied to parameters no. 5 (scanning strategies 5.2–5.6)

No.	*t* [mm]	h [μm]	pd [μm]	ext [μs]	v [mm/s]	lp [W]	E [J/mm^3]
R1	25	30	20	20	1,000	25	33.3
R2	25	30	60	20	3,000	75	33.3

Parameters no. 3

Based on obtained results for Parameters no. 1 and no. 2, we have selected new set of parameters. Followed modifications compared to Parameters no. 2 were implemented:

- Hatch distance was decreased.
- Energy density was decreased (below 60 J/mm^3).
- Scanning speed was increased.

Different scanning strategies including SM and multiple meltings (2–3 scanning of each layer) were applied. No rotation for these additional meltings (remeltings) was applied for Parameters no. 3. The scanning vector rotation of 45° was applied just between successive layers after spreading fresh powder (Figure A1 in the manuscript). Six sets of platforms with samples were fabricated with Parameters no. 3 presented in Table A4.

Figure A1 Realizer SLM50 building platform with NiTi samples made with Parameters no. 1 set. Majority of samples are overheated (red arrows)

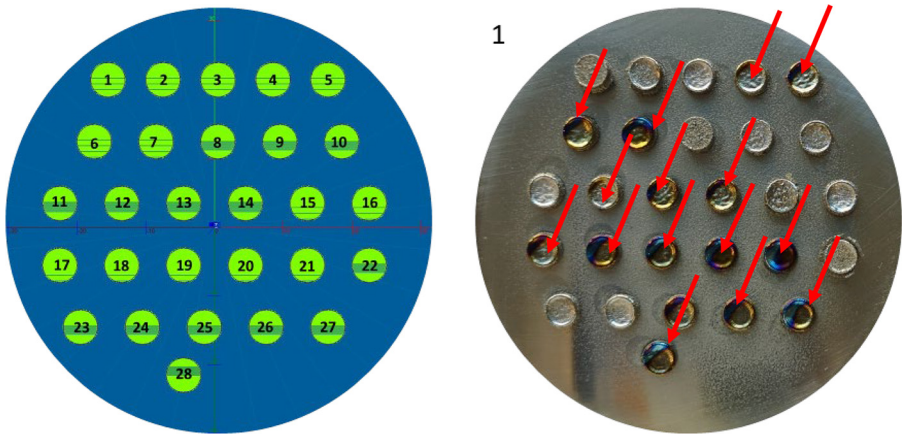

Figure A2 Microstructure of samples no. 1, 8, 15 and 22 fabricated with Parameters no. 1

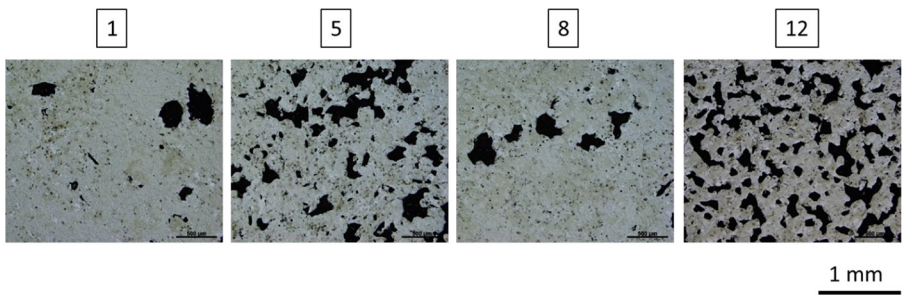

Figure A3 Realizer SLM50 building platforms with NiTi samples made with the set of Parameters no.2 with scanning strategies 2.1–2.5

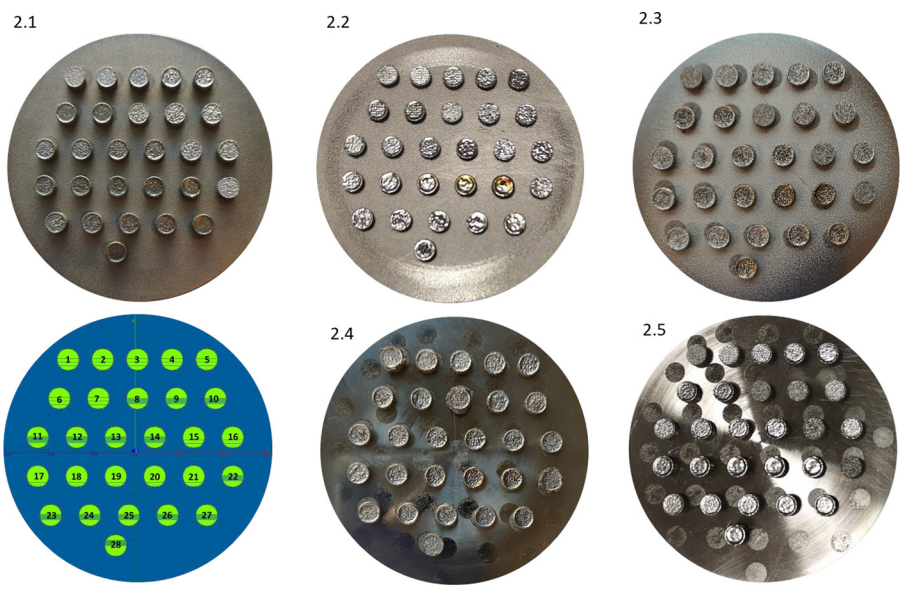

First, SM was performed (3.1) for 24 samples fabricated with parameters presented in Table A4. Then, for scanning strategy 3.2, double melting was applied – each layer was scanned twice with the same parameters as first melt run (1–24 Table A4). Results showed that the energy delivered to the material was to high and resulted in the failure of most of the samples (overheating and delamination). Based on those results, we have determined new parameters for additional melting (Table A5). Additional melting was performed before (premelting: 3.3) and after (remelting: 3.4) melting with the

Figure A4 Microstructure of samples no. 1, 5, 8 and 12 fabricated with Parameters no. 2 and scanning strategies 2.1–2.5

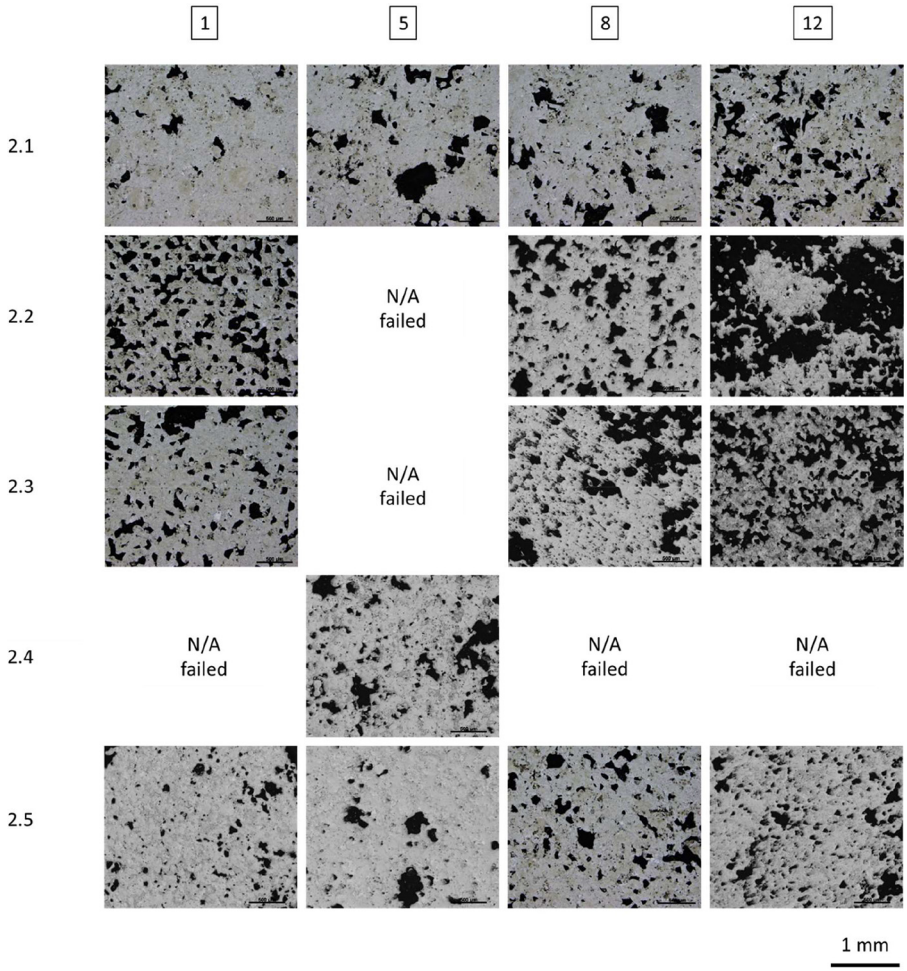

base (SM) parameters (presented in Table A4). Moreover, both premelting and remelting were also applied with base (SM – Table A4) parameters (3.5). Results showed that premelting did not provide good printability; thus, in further studies, only remelting was implemented. Triple melting, including SM (parameters 1–24 Table A4) and double remelting (parameters P/R Table A5) was applied (3.6).

List of the variations (scanning strategies) for Parameters no. 3 (no rotation for additional melting (remelting) before spreading fresh powder):

3.1. SM.
3.2. Double melting: 2x single melting.
3.3. Double melting: premelting (P/R) and single melting.
3.4. Double melting: single meltings and remelting (P/R).
3.5. Triple melting: premelting (P/R), single melting and remelting (P/R).
3.6. Triple melting: single melting and 2x remelting (P/R).

Fabricated samples on the platforms along with platforms numbers and the marking of samples on the platforms are presented in Figure A5:

Metallographic observations of polished samples made with Parameters no. 3 and melting strategies 3.1–3.6 are shown in Figure A6. Nevertheless, due to the high porosity and delamination, some of the samples could not be removed from the platform in a form that allows the preparation of metallographic samples (have been damaged when removed from the building platform). The samples that could not be successfully removed from the platform were eliminated from further analysis. Moreover, the samples that failed in the early stage of fabrication (after few layers) was not analyzed.

Parameters no. 4

Based on obtained results for Parameters no. 3, we have selected new set of Parameters 4, which aims to further decrease of samples porosity. Followed modifications compared to Parameters no. 3 were implemented:

- Hatch distance was decreased.
- Laser power was decreased and increased.

Moreover, two different parameters of remelting, R_a and R_b, was applied (Table A7).

First, SM was performed (4.1) for 24 samples fabricated with parameters presented in Table A6. Second, remelting with parameters R_a and R_b was performed one, two and three times for scanning strategies 4.2–4.7.

As previously, no rotation (between first and following scanning) was applied for any of the scanning strategy. The

Figure A5 Realizer SLM50 building platforms with NiTi samples made with the set of Parameters no.3 with scanning strategies 3.1–3.6

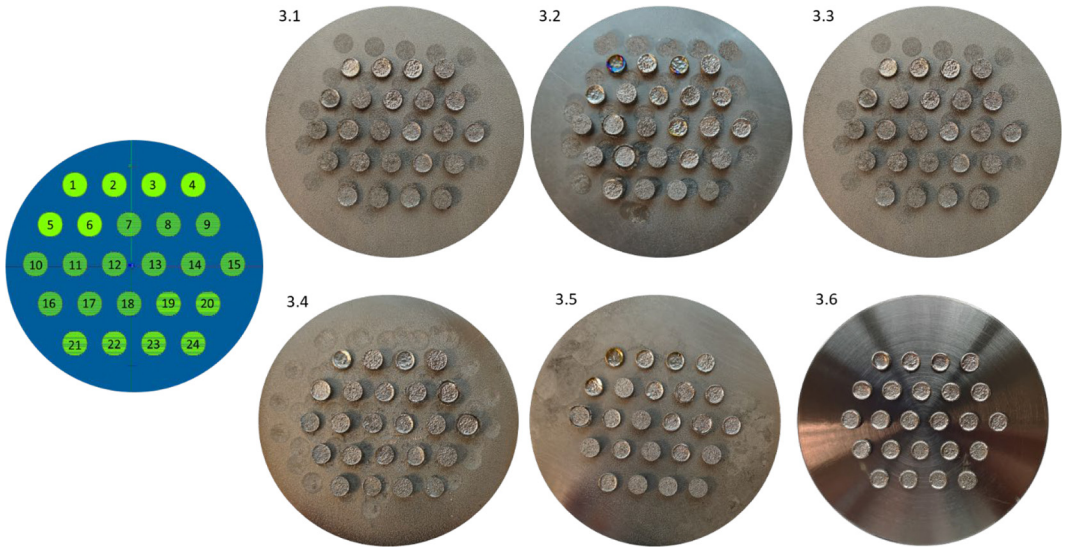

Figure A6 Microstructure of samples no. 2, 6, 8 and 12 fabricated with Parameters no. 3 and scanning strategies 3.1–3.6

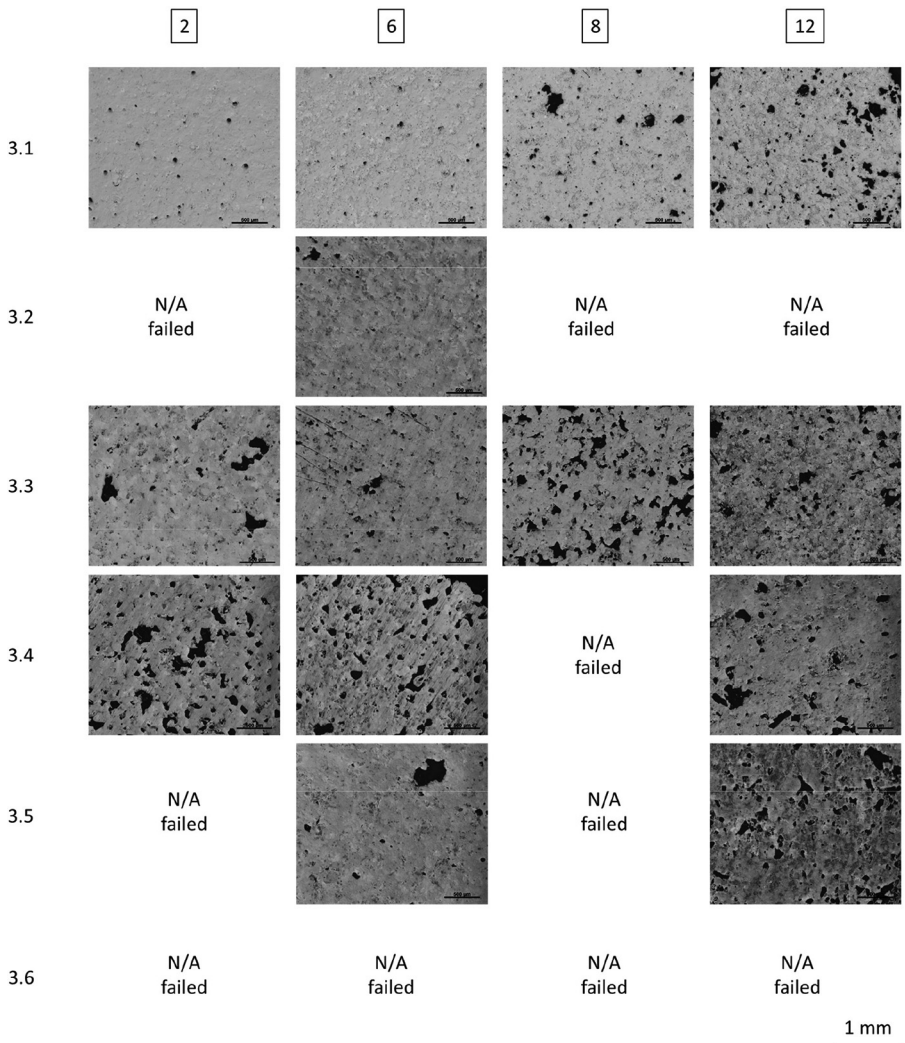

rotation of 45° scanning vector between successive layers was applied (Figure A1 in the manuscript).

List of the variations (scanning strategies) for Parameters no. 4 (no rotation applied):

4.1. Single melting.
4.2. Single melting and remelting R_a.
4.3. Single melting and 2x remelting R_a.
4.4. Single melting and 3x remelting R_a.
4.5. Single melting + remelting R_b.
4.6. Single melting + 2x remelting R_b.
4.7. Single melting + 3x remelting R_b.

Fabricated samples on the platforms along with platforms numbers and the marking of samples on the platforms are presented in Figure A7:

Metallographic observations of polished samples were performed (Figure A8). Nevertheless, due to the high porosity and delamination, some of the samples could not be removed from the platform in a form that allows the preparation of metallographic samples (have been damaged when removed from the building platform). The samples that could not be successfully removed from the platform were completely eliminated from further analysis. Moreover, the samples that failed in the early stage of fabrication (after few layers) was not analyzed.

Parameters no. 5

Based on obtained results for Parameters no. 4, we have selected new set of parameters. Followed modification compared to Parameters no. 4 was implemented:

- Hatch of 50 μm was added and 100 μm was deleted.

First, SM was performed (5.1) for 27 samples fabricated with parameters presented in Table A8. Second, remelting with parameters R1 and R2 was performed one and two times for scanning strategies 5.2–5.5. Triple remelting with R1 parameters was not successful and samples failed in the early stage of the fabrication process (5.6). The results showed that after producing only a few layers (approximately 20–30 layers, that was about 0.5–0.75 mm), the side cracks caused them to wrap and detach from the substrate and further production was not possible. The results were not presented within the manuscript. Double remelting with R2 parameters caused excessive melting (overheating) of some of the samples and defects increased; thus, triple remelting was not applied.

As previously, no rotation (between first and following scanning) was applied for any of the scanning strategy. The rotation of 45° scanning vector between successive layers was applied (Figure 1 in the manuscript).

List of the variations (scanning strategies) for Parameters no. 5:

5.1. Single melting.
5.2. Single melting + remelting R1.
5.3. Single melting + 2x remelting R1.
5.4. Single melting + remelting R2.
5.5. Single melting + 2x remelting R2.
5.6. Single melting + 3x remelting R1.

Fabricated samples on the platforms along with platforms numbers and the marking of samples on the platforms are presented in Figure A9:

The results obtained within Parameters no. 5 and scanning strategies 5.1–5.5 were satisfying and allowed to fabricate high quality samples with high density (above 99%). It was observed that remelting improves the quality of fabricated coupons (decrease porosity and number of cracks) and the parameters of remelting highly influence the results (differences were observed for R1 and R2 remelting parameters). Since scanning strategy 5.6 did not allow for the fabrication of any sample (excessive overheating and detaching samples from the platform), it was excluded from further analysis. The variations observed for using different scanning strategies 5.1–5.5 encouraged us to perform a more detailed analysis of the fabricated samples. The analysis was presented within the manuscript.

Figure A7 Realizer SLM50 building platforms with NiTi samples made with the set of Parameters no.3 with scanning strategies 4.1–4.7

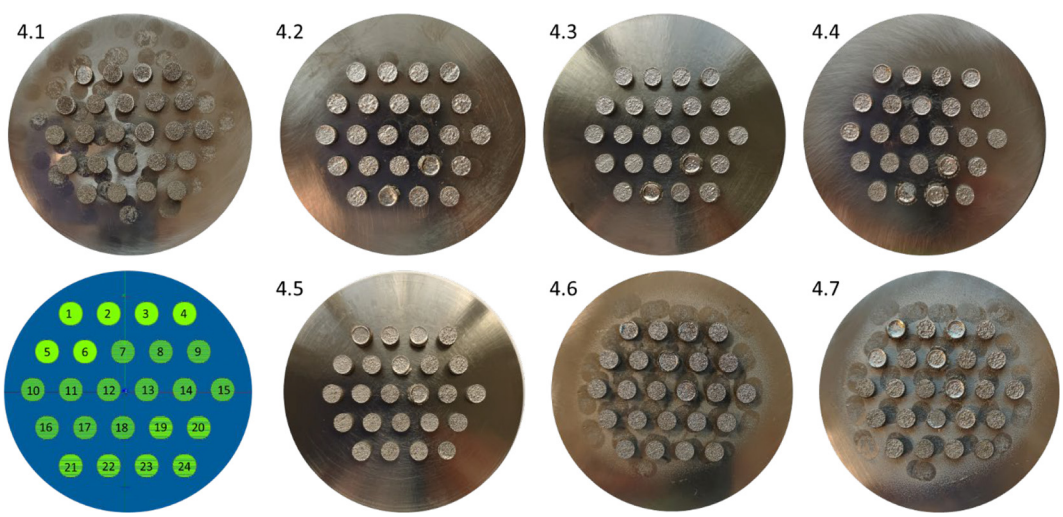

Figure A8 Microstructure of samples no. 2, 6, 8 and 12 fabricated with Parameters no. 4 and scanning strategies 4.1–4.7

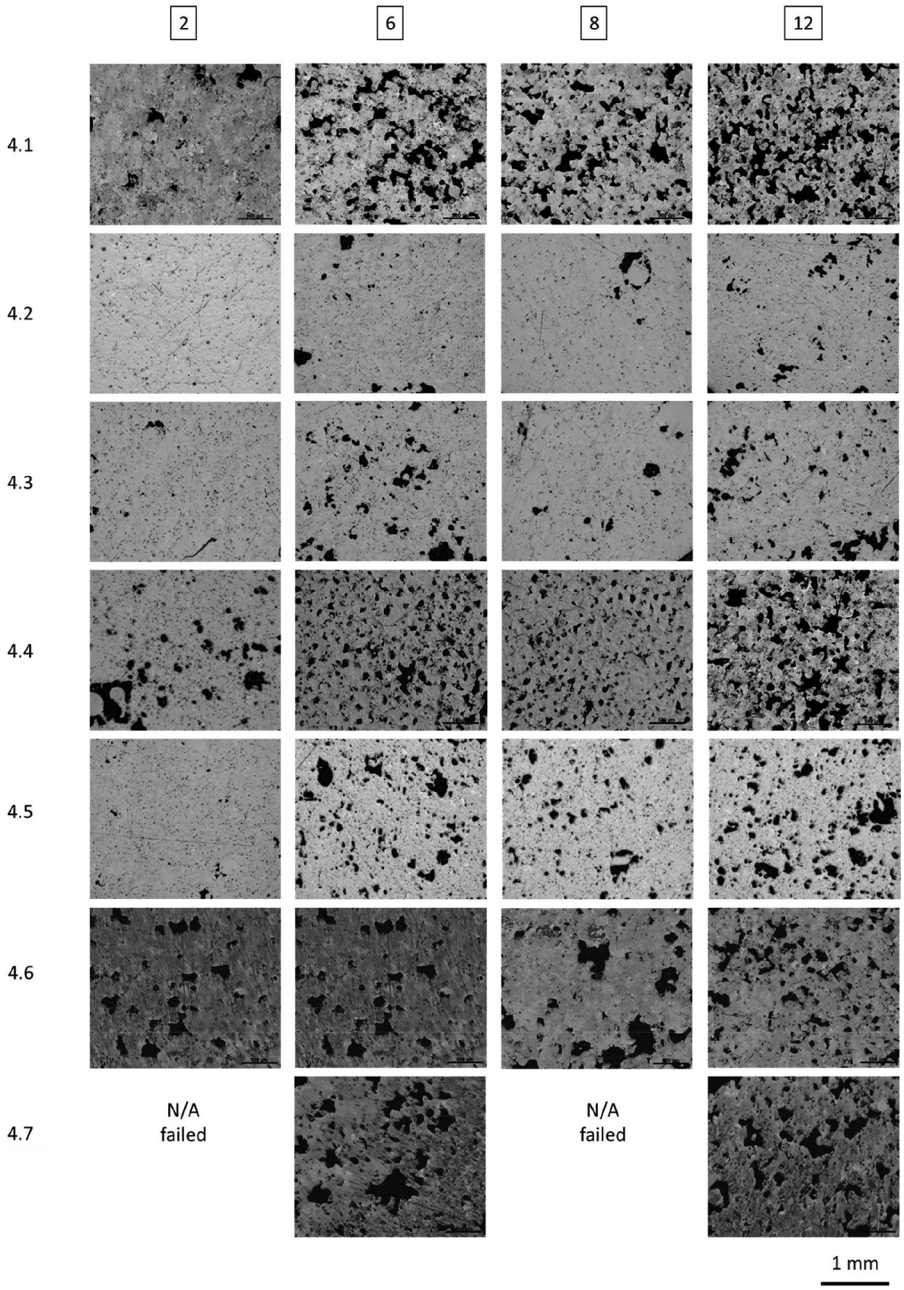

Figure A9 Realizer SLM50 building platforms with NiTi samples made with the set of Parameters no.5 with scanning strategies 5.1–5.6

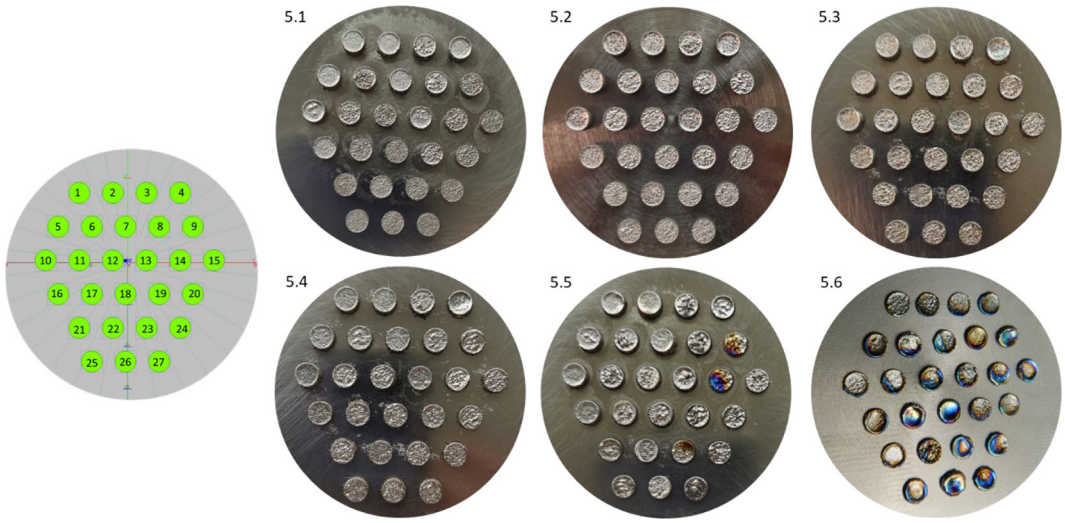

Appendix 2

Table A10 Relationship between relative density and energy density for NiTi manufactured with elementally blended powders (values for Figure A6 in the manuscript)

Energy density [J/mm^3]	Material density [%]				
	Single melting (SM)	SM + single remelting R1	SM + double remelting R1	SM + single remelting R2	SM + double remelting R2
80	94.90	96.00	97.56	97.55	97.35
73	92.84	N/A	N/A	97.44	97.40
67	91.10	94.90	94.15	98.19	98.34
53	92.45	94.00	94.46	97.19	96.89
49	93.19	93.27	93.36	96.10	96.54
48	94.84	94.11	93.92	96.31	97.01
44	83.44	88.98	90.68	94.08	94.32
44	85.11	95.58	95.89	95.31	96.44
40	79.74	87.19	85.88	94.08	91.32
40	94.39	96.77	95.46	96.60	97.50
37	81.34	92.80	92.95	95.89	95.30
34	93.82	96.16	92.58	93.17	96.65
33	76.87	N/A	N/A	92.34	92.74
32	89.62	94.51	89.49	94.64	94.12
31	94.85	97.63	N/A	94.58	96.93
29	78.94	N/A	N/A	90.44	N/A
29	92.88	95.24	N/A	92.04	93.63
27	85.97	97.34	92.22	88.75	88.65
24	71.61	93.28	N/A	90.22	82.39
23	81.18	93.43	N/A	88.52	88.40
22	68.12	81.50	89.92	81.66	83.32
21	78.41	96.71	N/A	92.89	85.73
20	57.29	93.52	92.56	85.22	91.92
19	76.36	94.84	N/A	85.25	89.96
17	67.47	96.00	N/A	81.15	80.78
16	72.50	90.82	N/A	84.69	89.01
14	65.02	93.85	N/A	80.93	80.50

Note: *N/A: sample failed during fabrication

Corresponding author

Agnieszka Chmielewska can be contacted at: agnieszka.chmielewska.dokt@pw.edu.pl